









Observational Signature of Circumstellar Interaction and ^{56}Ni -mixing in the Type II Supernova 2016gfy

Avinash Singh^{1,2} , Brajesh Kumar¹ , Takashi J. Moriya³ , G. C. Anupama¹ , D. K. Sahu¹, Peter J. Brown⁴ , Jennifer E. Andrews⁵ , and Nathan Smith⁵

¹ Indian Institute of Astrophysics, Koramangala 2nd Block, Bengaluru 560034, India; avinash21292@gmail.com, avinash.singh@iiap.res.in

² Joint Astronomy Programme, Department of Physics, Indian Institute of Science, Bengaluru 560012, India

³ Division of Science, National Astronomical Observatory of Japan, National Institutes of Natural Sciences, 2-21-1 Osawa, Mitaka, Tokyo 181-8588, Japan

⁴ Department of Physics and Astronomy, George P. and Cynthia Woods Mitchell Institute for Fundamental Physics & Astronomy, Texas A&M University, 4242 TAMU, College Station, TX 77843, USA

⁵ Steward Observatory, University of Arizona, 933 North Cherry Avenue, Tucson, AZ 85721, USA

Received 2019 April 10; revised 2019 July 2; accepted 2019 July 2; published 2019 September 4

Abstract

The optical and ultraviolet broadband photometric and spectroscopic observations of the Type II supernova (SN) 2016gfy are presented. The V -band light curve (LC) shows a distinct plateau phase with a slope of $s_2 \sim 0.12 \text{ mag (100 day)}^{-1}$ and a duration of 90 ± 5 days. Detailed analysis of SN 2016gfy provided a mean ^{56}Ni mass of $0.033 \pm 0.003 M_{\odot}$, a progenitor radius of $\sim 350\text{--}700 R_{\odot}$, a progenitor mass of $\sim 12\text{--}15 M_{\odot}$, and an explosion energy of $(0.9\text{--}1.4) \times 10^{51} \text{ erg s}^{-1}$. The P-Cygni profile of $\text{H}\alpha$ in the early-phase spectra ($\sim 11\text{--}21$ days) shows a boxy emission. Assuming that this profile arises from the interaction of the SN ejecta with the pre-existing circumstellar material (CSM), it is inferred that the progenitor underwent a recent episode (30–80 yr prior to the explosion) of enhanced mass loss. Numerical modeling suggests that the early LC peak is reproduced better with an existing CSM of $0.15 M_{\odot}$ spread out to ~ 70 au. A late-plateau bump is seen in the VRI LCs during $\sim 50\text{--}95$ days. This bump is explained as a result of the CSM interaction and/or partial mixing of radioactive ^{56}Ni in the SN ejecta. Using strong-line diagnostics, a subsolar oxygen abundance is estimated for the supernova H II region ($12 + \log(\text{O}/\text{H}) = 8.50 \pm 0.11$), indicating an average metallicity for the host of an SN II. A star formation rate of $\sim 8.5 M_{\odot} \text{ yr}^{-1}$ is estimated for NGC 2276 using the archival *GALEX* FUV data.

Key words: galaxies: individual (NGC 2276) – supernovae: general – supernovae: individual (SN 2016gfy)

Supporting material: data behind figures

1. Introduction

Core-collapse supernovae (CCSNe) are the result of gravitational core-collapse in massive stars with zero age main sequence (ZAMS) mass $\gtrsim 8 M_{\odot}$ (Heger et al. 2003; Smartt 2009). SNe II (II-P and II-L) form the segment of CCSNe that display eminent P-Cygni profiles of hydrogen in their observed spectra (Minkowski 1941; Filippenko 1997) whereas the others belong to the class of stripped envelope SNe. SNe II have been a subject of extensive study due to their majority in the class of CCSNe and thus has resulted in unveiling various correlations between the physical parameters (Hamuy 2003; Anderson et al. 2014; Spiro et al. 2014; Valenti et al. 2015).

SNe II that retain a large hydrogen envelope at the epoch of explosion show a “plateau” in their light curve (LC) and form the most common subtype, SNe II-P (Li et al. 2011). On the other hand, the ones that show a “linear” decline past the maximum light belong to the subtype, SNe II-L (Barbon et al. 1979; Patat et al. 1994; Arcavi et al. 2012). The plateau is an optically thick phase of almost constant luminosity characterized by the recombination of hydrogen, lasting an average of ~ 84 days (see optically thick phase duration (OPTd) in Anderson et al. 2014). Patat et al. (1994) differentiated Type II-P and II-L SNe based on their decline rates in the B -band and classified SNe II-P as having $\beta_{100}^B < 3.5 \text{ mag (100 day)}^{-1}$. However, recent sample studies of Anderson et al. (2014), Sanders et al. (2015), and Valenti et al. (2016) have argued that the class of Type II-P and II-L SNe form a continuous distribution and do not belong to distinct classes. According to

these authors, Type II-P and II-L SNe show a continual trend in decline rates and can be accredited to the differing hydrogen envelope mass (Faran et al. 2014a; Valenti et al. 2015; Singh et al. 2018), which can be attributed to the higher mass-loss rate associated with the massive progenitors of SNe II-L in comparison with SNe II-P (Elias-Rosa et al. 2011, and references therein).

Observational studies on metallicity of the host environment of CCSNe have helped in furnishing constraints on the progenitor properties (Prieto et al. 2008; Kuncarayakti et al. 2013a, 2013b; Taddia et al. 2015; Anderson et al. 2016, and references therein). The modeling of SN II atmospheres have shown a palpable dependence of metal-line strengths on the metallicity of the progenitor (Kasen & Woosley 2009; Dessart et al. 2013, hereafter KW09 and D13, respectively). The temporal evolution of the photosphere during the plateau phase describes the composition of the progenitor and hence the metal lines can help constrain the metallicity of the progenitor (Dessart et al. 2014; Anderson et al. 2016, hereafter D14 and A16, respectively). The increasing metallicity amidst the model progenitors (D13) of SNe II display stronger (large equivalent-width, EW) metal-line features at a given epoch.

An upper limit of $25 M_{\odot}$ has been predicted by hydrodynamical modeling of red supergiants (RSGs) to retain its hydrogen envelope and explode as SNe II (Heger et al. 2003; Bersten et al. 2011; Morozova et al. 2015). The inhomogeneity in RSGs results from differences in initial masses, metallicity, and mass-loss rates. Direct detection of progenitors in the nearby galaxies (distance ≤ 25 Mpc) have

been possible in the recent past using the pre-explosion images obtained from the *Hubble Space Telescope* and other big telescopes (Van Dyk et al. 2019, and references therein). The inferred masses of progenitors from direct detection lie in the range of $\sim 9 - 17 M_{\odot}$ (Smartt 2009), which falls significantly short of the upper limit derived from modeling. This is termed as the RSG problem and has been explained as a result of “failed SNe,” which occurs in the higher end of the RSG mass range (Woosley & Heger 2012; Lovegrove & Woosley 2013; Horiuchi et al. 2014). Alternatively, pre-SN mass loss can also affect the estimates of progenitor mass due to anomalous dust correction (Kochanek et al. 2012; Walmswell & Eldridge 2012). Davies & Beasor (2018) explains this as a result of uncertainties in the mass–luminosity relationship and small number statistics.

In the absence of direction detection, the progenitor properties of the SN can be inferred from the explosion properties such as explosion energy, ^{56}Ni mass etc. These estimates are dependent on the distance to the SN. SNe II have shown promise as a standard candle for estimating distances to extragalactic sources. Due to increased star formation rate (SFR) with higher redshifts (up to ~ 2 , Dickinson et al. 2003), the abundance of SNe II at higher redshifts than SNe Ia make them an important diagnostic for estimating distance and potentially determining cosmological parameters. However, SNe II being fainter than SNe Ia argues against their importance at higher redshifts although the different systematics of using them as distance indicators makes them important. The most commonly used techniques are the expanding photosphere method (Kirshner & Kwan 1974, EPM), the standard candle method (Hamuy & Pinto 2002, SCM), the photospheric magnitude method (Rodríguez et al. 2014, PMM) and the photometric color method (de Jaeger et al. 2015; PCM). The EPM is a geometrical technique used to derive distances using the angular and the photospheric radii of the SN. The SCM is built on the observed correlation of the expansion velocity and the luminosity at an epoch during the plateau phase of an SN II. The PMM employs the precise knowledge of the explosion epoch, expansion velocity, and the extinction corrected magnitudes whereas the PCM utilizes the correlation between luminosity, color, and the late-plateau decline rate, to compute the distance to an SN II.

The study of SNe II enables understanding the diversity among their progenitors and one such object is presented here. SN 2016gfy was discovered by Alessandro Dimai on 2016 September 13.10 UT in the galaxy NGC 2276 at an unfiltered apparent magnitude of ~ 16.3 mag (Dimai 2016). It lies $18''\text{E}$ and $20''\text{N}$ from the nucleus of the host. A spectrum obtained by the NOT Unbiased Transient Survey on 2016 September 15.25 UT, displayed a blue continuum with broad Balmer emission lines classifying it as a young SN II (Kuncarayakti et al. 2016). Brief details on SN 2016gfy are given in Table 1.

We present here detailed photometric and spectroscopic analysis of the Type II-P SN 2016gfy. The temporal evolution of the SN is studied in detail and its explosion parameters are determined. The properties of the host galaxy NGC 2276 are also studied and the progenitor parameters estimated. The properties of SN 2016gfy are compared with SNe II from the literature whose details are presented in Table 5 in Appendix A.

Table 1
Brief Details of SN 2016gfy and Its Host NGC 2276

Parameters	Value	References
<i>SN 2016gfy</i> :		
R.A. (J2000)	$\alpha = 07^{\text{h}}26^{\text{m}}43^{\text{s}}.67$	3
Decl. (J2000)	$\delta = +85^{\circ}45'51''.70$	3
Discovery date	2016 Sep 13.10 UT	3
Explosion date	2016 Sep 9.90 UT	1
Total reddening	$E(B - V) = 0.21 \pm 0.05$ mag	1
<i>NGC 2276</i> :		
Type	SAB(rs)c	2
R.A. (J2000)	$\alpha = 07^{\text{h}}27^{\text{m}}14^{\text{s}}.36$	2
Decl. (J2000)	$\delta = +85^{\circ}45'16''.40$	2
Redshift	$z = 0.008062 \pm 0.000013$	2
Distance	$D = 29.64 \pm 2.65$ Mpc	1
Distance modulus	$\mu = 32.36 \pm 0.18$ mag	1

References. (1) This paper; (2) de Vaucouleurs et al. (1991); (3) Dimai (2016).

2. Data Acquisition and Reduction

2.1. 2 m Himalayan Chandra Telescope (HCT)

The photometric and spectroscopic follow-up of SN 2016gfy with the Himalayan Faint Object Spectrograph Camera (HFOSC) mounted on the 2 m HCT, Indian Astronomical Observatory (IAO), Hanle, India began on 2016 September 13.74 (JD 2,457,645.24), roughly ~ 15 hr from discovery. Broadband photometric monitoring was carried out in Bessell *UBVRI* at 42 epochs and the spectroscopic observations⁶ were performed on 33 epochs using grisms Gr7 (3500–7800 Å, $R \sim 500$) and Gr8 (5200–9250 Å, $R \sim 800$).

Landolt field PG0231+051 (Landolt 1992) was observed on photometric nights of 2016 September 20, October 4 and December 5 for the photometric calibration of the SN field. Template subtraction was carried out due to significant contamination from the host galaxy, the details of which are given in Appendix A. The spectra from the two grisms were combined after scaling to a weighted mean using a common overlapping region in the vicinity of a flat continuum. A detailed description on the data reduction can be found in Kumar et al. (2018), Sahu et al. (2018), and Singh et al. (2018).

2.2. 6.5 m Multiple Mirror Telescope (MMT)

Medium-resolution spectra was obtained with the Bluechannel (BC) spectrograph mounted on the 6.5 m MMT (Schmidt et al. 1989) using the 1200 line/mm grating centered at 6300 Å. These spectra were reduced using standard techniques in PyRAF (Science Software Branch at STScI 2012), including bias subtraction, flat-fielding, wavelength calibration using arc lamps, and flux calibration using standard stars observed on the same nights at similar airmass. Observations were obtained with the slit aligned along the parallactic angle to minimize differential light losses (Filippenko 1982).

2.3. SWIFT Ultraviolet/Optical Telescope (UVOT)

SN 2016gfy was also observed with the Neil Gehrels Swift Observatory (Gehrels et al. 2004). Observations with the

⁶ The slit orientation during the spectroscopic follow-up of SN 2016gfy was along the E–W direction.

UVOT (Romig et al. 2005) began 2016 September 15 UT. Data reduction utilized the pipeline of the Swift Optical Ultraviolet Supernova Archive (Brown et al. 2014) including the revised Vega-system zero-points of Breeveld et al. (2011). The underlying count rates from the host galaxy were measured from images obtained on 2018 March 19 and subtracted from the photometry.

3. Host Galaxy—NGC 2276

The host galaxy of SN 2016gfy, NGC 2276 is a face-on starburst spiral galaxy interacting with the elliptical galaxy NGC 2300 ($d \sim 30$ Mpc, Mould et al. 2000). Ram-pressure and viscous stripping form the basis for its distorted morphology and the increased SFR in the galaxy (Davis et al. 1997; Wolter et al. 2015; Tomičić et al. 2018). Measurements of X-ray gas on the disk of NGC 2276 have yielded a low metallicity ($\sim 0.1 Z_{\odot}$) with no appreciable differences between the edges of the galaxy (toward or away from the interaction, Rasmussen et al. 2006).

3.1. SFR from GALEX Archival Image

Flux-normalized and background-subtracted FUV intensity image of NGC 2276 was obtained from GALEX Catalog Search⁷ and aperture photometry was performed with an elliptical aperture using the *photutils* python package (Bradley et al. 2017). The galaxy is surrounded by bright foreground stars and hence an aperture smaller than the isophotal diameter (at $B = 25$ mag arcsec⁻²) was used in computing the net flux from the galaxy. The flux obtained was converted into the AB magnitude system of Oke & Gunn (1983) using the zero-point in Morrissey et al. (2007). The correction for Galactic and internal extinction was applied assuming Fitzpatrick (1999) extinction law with the help of the York Extinction Solver (McCall 2004) to obtain the final FUV magnitude, $m_{\text{FUV}} \sim 13.11$ mag.

An SFR of $\sim 8.5 M_{\odot} \text{ yr}^{-1}$ is estimated for NGC 2276 using its FUV magnitude (Karachentsev & Kaisina 2013). Using an $H\alpha$ flux of 6.3×10^{-12} erg cm⁻² s⁻¹ (Davis et al. 1997) for NGC 2276 and the relation by Kennicutt (1998), an SFR of $\sim 5.2 M_{\odot} \text{ yr}^{-1}$ is determined. The SFR values obtained above are consistent with the values from the literature for NGC 2276 (Tomičić et al. 2018).

The galaxy has been a host to five reported SNe (prior to SN 2016gfy), namely SN 1962Q (Iskudaryan & Shakhbazyan 1967), SN 1968V⁸ (Shakhbazyan 1968), SN 1968W (Iskudarian 1968), SN 1993X (see footnote 8; Treffers et al. 1993), and SN 2005dl (see footnote 8; Dimai et al. 2005). Of the six SNe, four are confirmed Type II (including SN 2016gfy), while the other two are unclassified. Hence, 4_{-0}^{+2} CCSNe have occurred in the last 57 yr leading up to 2019, giving us an observed supernova rate (SNR) of $0.070_{-0}^{+0.035}$ CCSNe yr⁻¹.

The relation between SNR and SFR was estimated using the BPASS v2.2 catalog (Eldridge et al. 2017; Stanway & Eldridge 2018) assuming the Chabrier initial mass function (Chabrier 2003). A mean SNR of ~ 0.009 CCSNe yr⁻¹ is expected for an SFR of $1 M_{\odot} \text{ yr}^{-1}$ for metallicities ranging from 0.1 (inferred from X-ray gas) to 0.8 (nuclear metallicity of NGC 2276) Z_{\odot} . This gives an SFR of $\sim 7.8 M_{\odot} \text{ yr}^{-1}$ for NGC 2276 and is consistent with the photometric estimates of SFR.

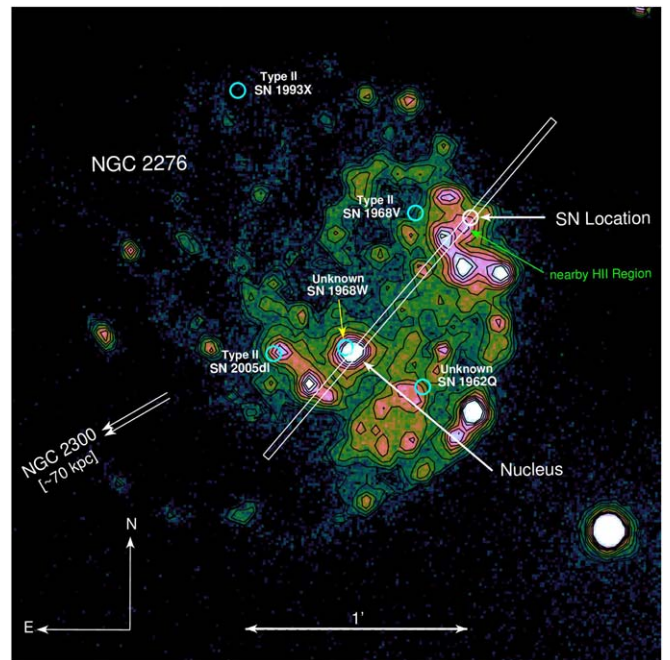


Figure 1. Narrowband $H\alpha$ image of the host galaxy NGC 2276 obtained from Epinat et al. (2008). The interacting galaxy NGC 2300 (Davis et al. 1997) is located SE of NGC 2276 at a projected distance of ~ 70 kpc. The nucleus and the location of SN 2016gfy is marked along with the five reported SNe in the galaxy and their subtypes (if known). Isointensity contours are shown in black to reveal regions of enhanced $H\alpha$ emission in the galaxy. The H II region closest to the SN location is indicated. The size of the circular markers depict the average seeing ($\sim 2''$) at the site of HCT. The slit orientation for the host environment spectrum (Section 3.3) is shown with a rectangular box. The image is shown in square-root intensity scale for clarity.

3.2. Parent H II Region

The observed $H\alpha$ luminosity in spiral galaxies trace the ionized regions produced by the radiation from massive OB stars ($> 10 M_{\odot}$). Hence, the $H\alpha$ line emission can help indicate the parent population of CCSNe (Kennicutt 1984). The $H\alpha$ map of NGC 2276 obtained from Epinat et al. (2008) is shown in Figure 1. The nearest H II region lies $\sim 2''$ away from SN 2016gfy signifying probable association and shares the property of the region.

3.3. Host Environment Spectroscopy

A Gr7 (3500–7800 Å) spectrum of the parent H II region of SN 2016gfy along with nucleus of the host galaxy NGC 2276 was obtained on 2018 October 31 by orienting the HFOOSC slit across the two locations as shown in Figure 1. Calibrated one-dimensional spectra corresponding to both the regions are shown in Figure 2. The spectra of the two regions exhibited prominent emission lines of $H\alpha$, $H\beta$, [N II] 6548, 6584 Å, [S II] 6717, and 6731 Å, whereas the [O III] 4959, 5007 Å lines were present only in the spectrum of the parent H II region.

To be able to use emission line diagnostics for determining the metallicity of the nucleus, other ionizing sources such as AGN contamination and shock-excitation must be ruled out (Taddia et al. 2015). The shorthand notation, $N2 \equiv \log([\text{N II}] \lambda 6584 / H\alpha)$, $O3 \equiv \log([\text{O III}] \lambda 5007 / H\beta)$, and $O3N2 \equiv \log([\text{O III}] \lambda 5007 / H\beta) / [\text{N II}] \lambda 6584 / H\alpha$ is used henceforth. The line ratios from the nucleus obey the relation, $O3 < 0.61 / ((N2 - 0.05) + 1.3)$ coined by Kauffmann et al. (2003) based on the BPT diagram

⁷ <http://galex.stsci.edu/GR6/?page=mastform>

⁸ Confirmed SNe II.

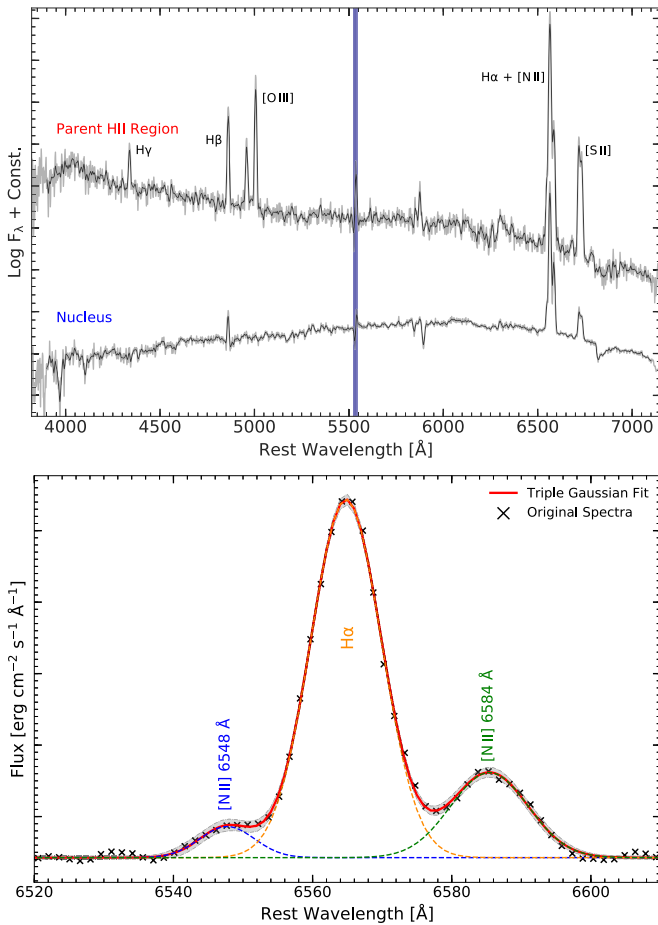


Figure 2. Top panel: spectrum of the nucleus of the host galaxy NGC 2276 and the parent H II region of the SN. Notable emission lines are labeled and the region shaded in dark blue indicates the artifact in our spectra. Bottom panel: a triple Gaussian fit to the H α (contaminated by the [N II] doublet) profile to compute the individual line fluxes.

(Baldwin et al. 1981) and confirms the star-forming nature of the nucleus without any significant AGN contamination.

The gas-phase oxygen abundances of these regions were computed from the N2 and the O3N2 indices using the relations from Pettini & Pagel (2004). An oxygen abundance of 8.61 ± 0.18 ($\sim 0.8 Z_{\odot}$) was estimated for the nucleus of NGC 2276 using the N2 diagnostic and a mean oxygen abundance of 8.50 ± 0.11 ($\sim 0.6 Z_{\odot}$) was estimated for the parent H II region using the N2 and O3N2 diagnostics. The lower metallicity of the parent H II region in comparison to the nucleus is consistent with radially decreasing metallicity gradients seen in galaxies (Henry & Worthey 1999). The abundance of the parent H II region indicates a subsolar oxygen abundance adopting a solar abundance of 8.69 ± 0.05 (Asplund et al. 2009). The use of emission line ratios in these diagnostics minimizes the need for precise extinction correction and flux calibration.

A mean oxygen abundance of ~ 8.49 was estimated by Anderson et al. (2016) for an unbiased sample of SNe II host H II regions. This indicates that the parent H II region of SN 2016gfy has an average oxygen abundance for the host of an SN II.

4. Estimate of Total Extinction and Distance

Extinction along the line of sight of SN 2016gfy is composed of reddening from the dust in the Milky Way

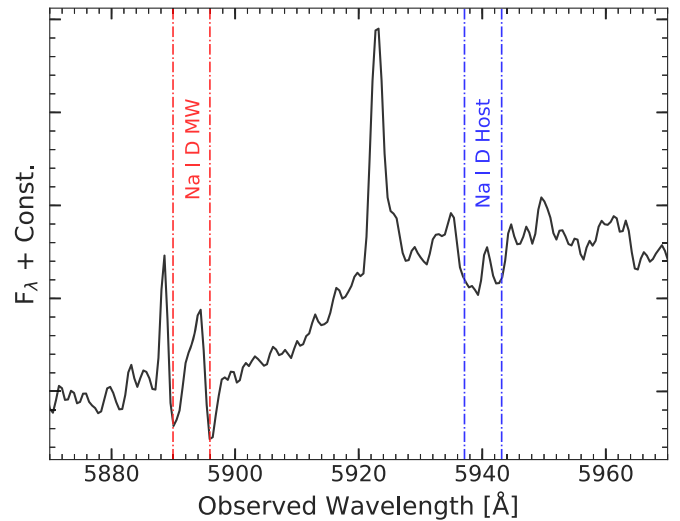


Figure 3. Na I D from the MW and the host galaxy NGC 2276 in the spectrum of ~ 175.5 days from MMT. The dashed-dotted lines indicate the rest-wavelength of the features.

(MW) and the host galaxy NGC 2276. A Galactic reddening of $E(B - V) = 0.0865 \pm 0.0018$ mag is obtained from the dust-extinction map of Schlafly & Finkbeiner (2011), which assumes the Fitzpatrick (1999) extinction law. To determine the strength of the Na I D feature, four early-phase spectra (4–18 days from the date of explosion, see Section 5.1) of SN 2016gfy were coadded. The equivalent width (EW) of Na I D as measured from the combined spectrum is $0.44 \pm 0.08 \text{ \AA}$ and gives an $E(B - V) = 0.06 \pm 0.01$ mag (Turatto et al. 2003) and 0.05 ± 0.01 mag (Poznanski et al. 2012). Hence, a mean Galactic reddening of $E(B - V) = 0.07 \pm 0.01$ mag is adopted in the direction of SN 2016gfy.

A weak Na I D is also identified at the redshift of the host galaxy and is seen superimposed over the P-Cygni profile from the SN (He I in the early phase and Na I D in the late phase). The composite spectra yields an Na I D EW of $0.89 \pm 0.13 \text{ \AA}$, which corresponds to an $E(B - V) = 0.13 \pm 0.02$ mag (Turatto et al. 2003) and 0.16 ± 0.07 mag (Poznanski et al. 2012). Host galaxy reddening was further confirmed using the “color method” proposed by Olivares et al. (2010) which postulates that the intrinsic $(V - I)$ color is constant for SNe II-P (i.e., $(V - I)_0 = 0.656$ mag) at the end of the plateau phase. Using the Galactic reddening corrected $(V - I)$ color prior to the end of the plateau phase (~ 80.8 days), an $E(B - V)_{\text{host}} = 0.14 \pm 0.11$ mag was obtained assuming a total-to-selective extinction ratio, $R_V = 3.1$. A mean reddening of $E(B - V) = 0.14 \pm 0.05$ mag is estimated for the host galaxy NGC 2276. These measurements were verified with the resolved Na I D in the medium-resolution spectrum obtained from MMT (see Figure 3).

The host extinction estimate was also verified using Balmer decrement (H α /H β ratio, Osterbrock 1989). Using Equation (4) from Domínguez et al. (2013), which assumes Case B recombination ($T \sim 10^4$ K and a large τ), the emission line flux ratios from the spectrum of the parent H II region gives an $E(B - V)_{\text{host}} \sim 0.13$ mag, confirming the estimate for the host reddening by other methods. A total reddening of $E(B - V) = 0.21 \pm 0.05$ mag is adopted for SN 2016gfy.

The distance to SN 2016gfy is estimated using various SCM techniques and is mentioned in Table 2. A mean SCM distance of 29.64 ± 2.65 Mpc ($\mu = 32.36 \pm 0.18$) is inferred for the host

Table 2
Distances Derived from SCM Analysis Using $H_0 = 73.52 \pm 1.62 \text{ km s}^{-1} \text{ Mpc}^{-1}$

Reference	Filter	α	β	γ	Epoch (days)	$V - I$ (mag)	App. Mag. (mag)	$v_{\text{Fe II}}$ (km s^{-1})	Distance (Mpc)
H04	V	6.25 ± 1.35	1.46 ± 0.15	...	t_0+50	...	16.26 ± 0.01	4272 ± 53	29.14 ± 3.49
	I	5.45 ± 0.91	1.92 ± 0.11	...	t_0+50	...	15.47 ± 0.02	4272 ± 53	29.19 ± 2.35
N06	I	6.69 ± 0.50	-17.49 ± 0.08	1.36	t_0+50	0.68 ± 0.02	15.47 ± 0.02	4272 ± 53	34.78 ± 2.21^a
P09	I	4.4 ± 0.6	-1.76 ± 0.05	0.8 ± 0.3	t_0+50	0.68 ± 0.02	15.47 ± 0.02	4272 ± 53	31.29 ± 3.40
O10	B	3.50 ± 0.30	-1.99 ± 0.11	2.67 ± 0.13	$t_{PT}-30$	0.83 ± 0.02	17.48 ± 0.02	3022 ± 42	27.00 ± 2.68
	V	3.08 ± 0.25	-2.38 ± 0.09	1.67 ± 0.10	$t_{PT}-30$	0.83 ± 0.02	16.29 ± 0.01	3022 ± 42	28.55 ± 2.13
	I	2.62 ± 0.21	-2.23 ± 0.07	0.60 ± 0.09	$t_{PT}-30$	0.83 ± 0.02	15.37 ± 0.02	3022 ± 42	27.50 ± 1.59
Mean									29.64 ± 2.65

Notes. H04—Hamuy (2004), N06—Nugent et al. (2006), P09—Pastorello et al. (2009), and O10—Olivares et al. (2010).

^a Exception: $H_0 = 70 \text{ km s}^{-1} \text{ Mpc}^{-1}$.

galaxy NGC 2276. The redshift ($z = 0.008062$) of NGC 2276 obtained from Epinat et al. (2008) corresponds to a luminosity distance estimate of 33.1 Mpc, with $H_0 = 73.52 \text{ km s}^{-1} \text{ Mpc}^{-1}$, $\omega_M = 0.286$, and $\omega_\Lambda = 0.714$ (see Table 7) and is slightly higher in comparison with the SCM distance. The uncertainty inferred in measuring SCM distances is 6%–9% (Olivares et al. 2010). It is to be noted that the SCM technique is sensitive to the progenitor mass and metallicity, which directly influence the mass of the hydrogen envelope (KW09).

5. Photometric Evolution

5.1. Epoch of Explosion and Rise Time

The first glimpse of light in SNe II is seen shortly after the shock breakout from the stellar surface (Colgate 1974; Falk & Arnett 1977). The flux in the early phase is governed by the rapid cooling of the SN ejecta and its expansion. To investigate the rise time, the shock breakout formulation from Waxman et al. (2007) was used as it approximates the ejecta as a blackbody emitting at a fixed wavelength with a dependence on the SN radius, $r \propto (t - t_0)^{0.8}$ and shock breakout temperature, $T \propto (t - t_0)^{0.5}$, where t_0 is the explosion epoch and $(t - t_0)$ denotes the time since the explosion epoch. The time-dependent diffusion relation from Arnett (1982) was used to account for the expansion phase, which represents the SN photosphere as a constant temperature blackbody expanding with a constant velocity and has a $(t - t_0)^2$ dependence. Together

$$f(t) = \frac{a_1}{e^{a_2(t-t_0)^{0.5}} - 1} (t - t_0)^{1.6} + \frac{a_3(t - t_0)^2}{\text{Arnett (1982)}}, \quad (1)$$

Waxman et al. (2007)

where a_1 , a_2 , and a_3 are free parameters. Trends in the past observational studies have obtained longer rise time for SNe II-L (possibly larger radii) than SNe II-P (Blinnikov & Bartunov 1993) as the photons take longer time to diffuse through the ejecta and are in coherence with the hydrodynamical simulations of Swartz et al. (1991). However, the longer rise time seen in SNe II-L can also be due to a higher E/M ratio and not necessarily larger radii (Rabinak & Waxman 2011).

The fits to the early time LC in *UBVRI* bands are shown in Figure 4. A mean explosion epoch (t_0^{Mean}) of JD 2,457,641.4 \pm 0.9 is estimated for SN 2016gfy from the functional fit in

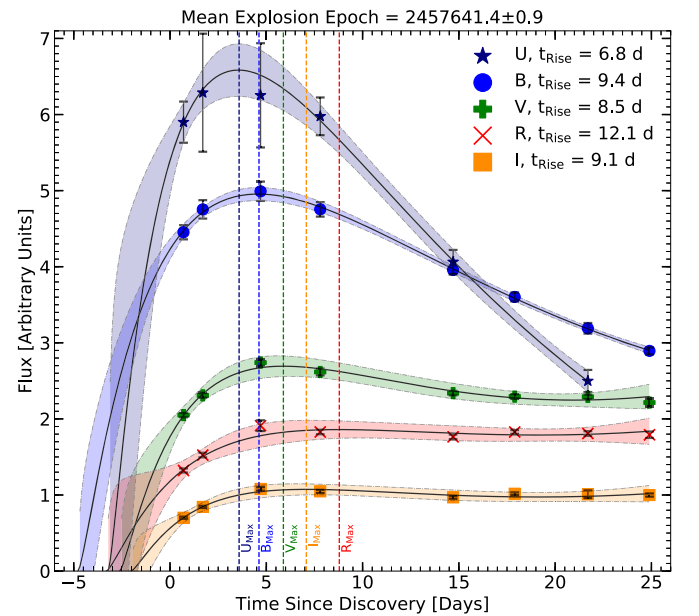


Figure 4. Fit to the early time LC (<25 days) of SN 2016gfy in Bessel *UBVRI* bands. The fit was performed using the relation in Cowen et al. (2010) and is shown with a solid line. 3σ confidence interval of the fits in different bands are shown in shaded colors.

UBVRI bands. The rise times inferred are mentioned in Table 3 and are intermediate to those of Type II-P (7.0 ± 0.3 days) and Type II-L (13.3 ± 0.6 days) SNe (Gall et al. 2015). The increase in rise time with wavelength seen for SN 2016gfy is consistent with the inference of González-Gaitán et al. (2015). For comparison, the rise times in *UBVRI* match the quintessential Type II-P SN 1999em in *UBV* (6, 8, and 10 days, Leonard et al. 2002b), but are significantly faster when compared with the bright Type II-P SN 2004et in *UBVRI* (9, 10, 16, 21, and 25 days, Sahu et al. 2006). Faster rise times in SNe II can be attributed to the presence of an immediate circumstellar material (CSM; Moriya et al. 2017, 2018; Morozova et al. 2017; Forster et al. 2018, see Figure 21).

5.2. Optical LCs

The *UBVRI* LCs of SN 2016gfy span ~ 4 –387 days from the date of explosion and are shown in the left panel of Figure 5.

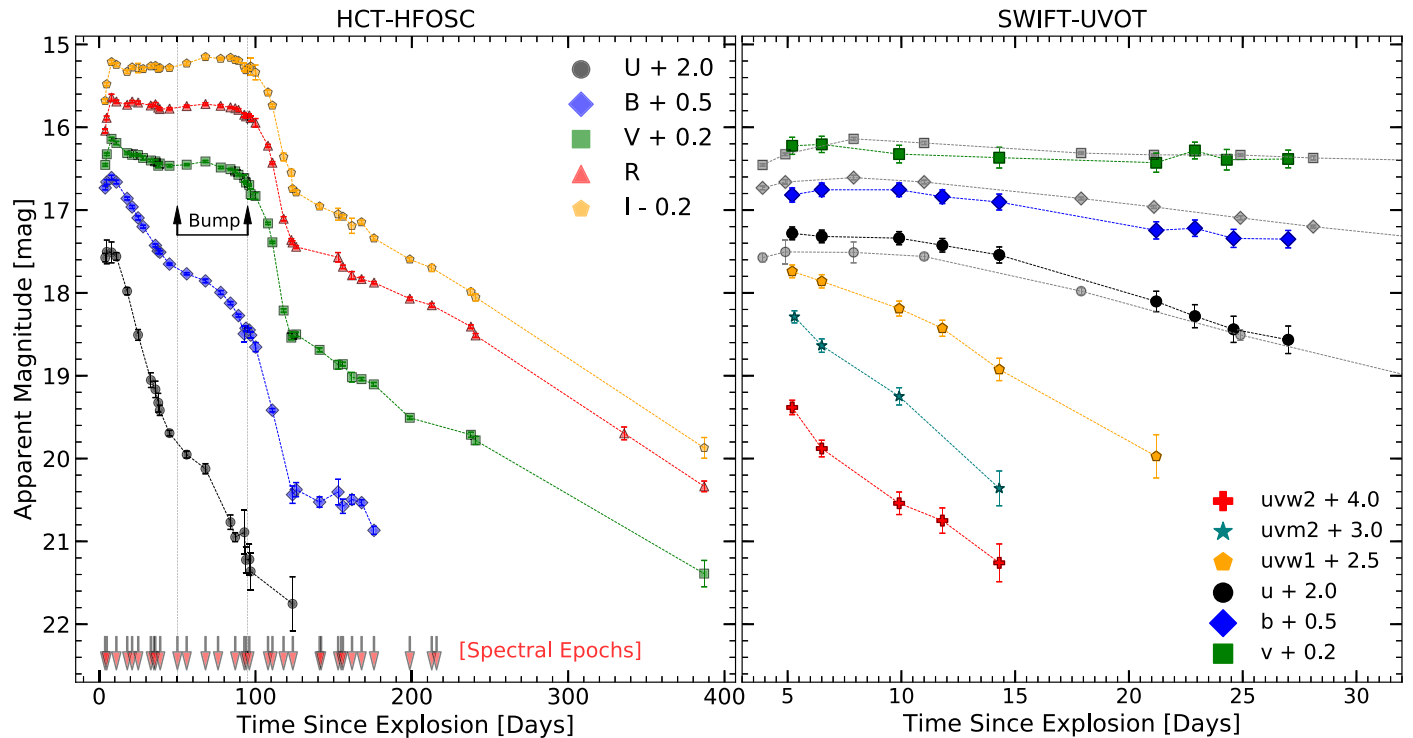


Figure 5. Apparent magnitude light curves of SN 2016gfy obtained from HCT-HFOSC and SWIFT-UVOT in the left and right panels respectively. Additionally, data from *UBV* filters (in gray) are also shown in the right panel. The “bump” in the *VRI* LC has been indicated. Offsets have been applied for clarity.

(The data used to create this figure are available.)

Table 3
Parameters Extracted from the Fit (Equation (1)) to the Early Time LC of SN 2016gfy

Filter	a_1 ($\times 10^{-15}$)	a_2	a_3 ($\times 10^{-18}$)	t_{Max} (JD)	$t_{\text{Max}} - t_0$ (days)	$t_{\text{Max}} - t_0^{\text{Mean}}$ (days)
<i>U</i>	2.75 ± 0.34	1.224 ± 0.042	-0.60	2457648.2	6.8 ± 0.5	6.8 ± 0.5
<i>B</i>	1.28 ± 0.07	1.057 ± 0.016	0.50	2457649.2	9.4 ± 0.3	7.8 ± 0.3
<i>V</i>	0.90 ± 0.11	1.155 ± 0.042	1.50	2457650.5	8.5 ± 0.4	9.1 ± 0.4
<i>R</i>	0.42 ± 0.11	1.028 ± 0.080	1.00	2457653.2	12.1 ± 0.8	12.0 ± 0.8
<i>I</i>	0.35 ± 0.06	1.148 ± 0.059	0.80	2457651.6	9.1 ± 0.4	10.3 ± 0.4

The *VRI* LCs of SN 2016gfy show four visually distinguishable phases: the rising phase (~ 10 days), the plateau phase (~ 10 – 90 days), the transition phase (~ 90 – 115 days), and the nebular phase (> 115 days). The rise to the maximum seen in *UBVRI* bands has been used in estimating the date of explosion in Section 5.1. The *B*-band magnitude declines by ~ 1.8 mag in the first 100 days, which is well within the value quoted (i.e., $\beta_{100}^B < 3.5$ mag) for SNe II-P by Patat et al. (1994). The late-plateau decline rates in *UBVRI* for SN 2016gfy are 2.94, 1.15, 0.12, -0.01 , and -0.27 mag (100 day) $^{-1}$. The *V*-band decline rate for SN 2016gfy is much lower in comparison to the luminous SNe II-P like SN 2013ab (0.92, Bose et al. 2015b), SN 2013ej (1.53, Bose et al. 2015a), and ASASSN-14dq (0.96, Singh et al. 2018), and is shown in Figure 6.

5.3. Swift UVOT LCs

Swift UVOT LCs shown in Figure 5 span the epochs ~ 5 – 27 days from the date of explosion and show faster decline in bluer bands as is expected for an SN II (Brown et al. 2007; Pritchard et al. 2014). The UV bands *uvw2*, *uvm2*, and *uvw1* do not cover the peak as the observations were triggered more than

2 days from discovery (> 5 days from explosion). The decline rates in *uvw2*, *uvm2*, and *uvw1* are 0.21, 0.23, and 0.14 mag (day) $^{-1}$ and are similar to the decline rates observed in other SNe II. The decline rate in *uvm2* is higher than in *uvw2*, contrary to the general anticorrelation of decline rates with wavelength. The faster *uvm2* decay results from the higher density of Fe II lines in the *uvm2* bandpass, which absorbs more effectively as the SN cools (see Figure 5 in Brown et al. 2007).

5.4. Bolometric LC

The pseudo-bolometric LC of SN 2016gfy was generated following the prescription in Singh et al. (2018) and integrating over the wavelength range 3100–9200 Å. A comparison of SN 2016gfy with other SNe II is shown in Figure 7. The peak bolometric luminosity of SN 2016gfy is $\sim 1.8 \times 10^{42}$ erg s $^{-1}$. The bolometric luminosity declines at the rate of 1.00 and 0.06 dex (100 days) $^{-1}$, respectively, during the early and late plateau phases, and 0.46 dex (100 days) $^{-1}$ during the nebular phase. The late-plateau phase shows a moderate bump (increase in flux), which is seen mostly in low-luminosity SNe II (e.g., SN 2005cs, Pastorello et al. 2009). The behavior of SN 2016gfy during the

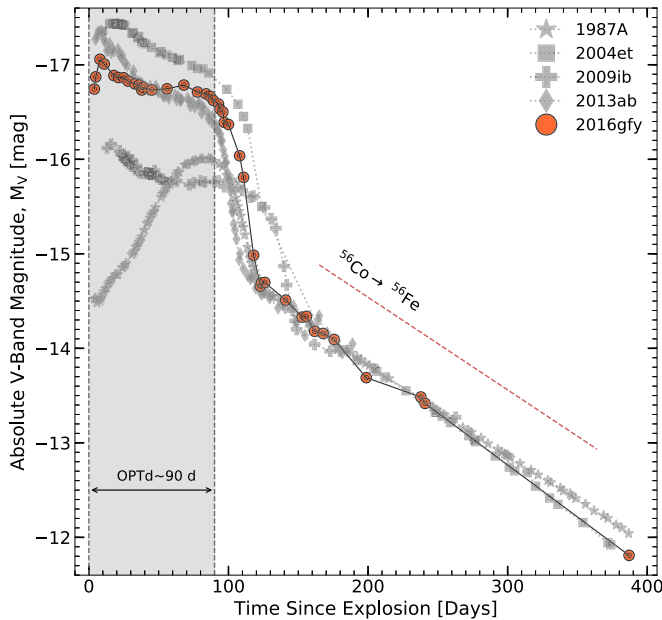


Figure 6. V-band absolute magnitude LC of SN 2016gfy in comparison with other SNe II-P. References: 1987A (Hamuy & Suntzeff 1990); 2004et (Sahu et al. 2006); 2009ib (Takáts et al. 2015); 2013ab (Bose et al. 2015b).

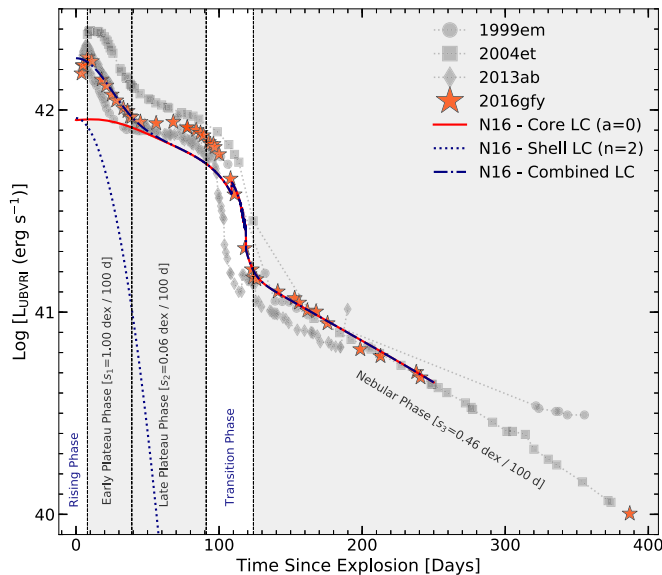


Figure 7. Pseudo-bolometric light curve of SN 2016gfy along with other SNe II. Dashed vertical lines show the epochs of transition between the different phases. The two-component fit from the analytic model of Nagy & Vinkó (2016) is also shown. References: 1999em (Leonard et al. 2002a); 2004et (Sahu et al. 2006); 2013ab (Bose et al. 2015b).

late-plateau phase is discussed in Section 8.2. The slow decline rate during the late-plateau phase is also a signature of low-mass progenitors in the modeled explosions of Sukhbold et al. (2016, hereafter S16), indicating a low-mass progenitor of SN 2016gfy.

5.5. Color Evolution

Evolution of intrinsic color terms $(U - B)_0$, $(V - R)_0$, $(uvw2 - uvw1)_0$, and $(uvw2 - v)_0$ of SN 2016gfy in comparison with other SNe II is shown in Figure 8. The $(U - B)_0$ evolution of SN 2016gfy does not follow other SNe II (except

SN 2004et); however, $(V - R)_0$ evolution shows no such differences. The significantly bluer color evolution in $U - B$ during the plateau is indicative of lower line blanketing in the blue region, consequently implying lower metallicity of the progenitor (D14) similar to SN 2004et (Jerkstrand et al. 2012). Even with a clear observable difference in the V-band LC of SN 2013ab and SN 2016gfy (due to the presence of a late-plateau bump in SN 2016gfy), we see insignificant differences in their $V - R$ color evolution. The $(uvw2 - uvw1)_0$ and $(uvw2 - v)_0$ colors of SN 2016gfy also show a bluer evolution in comparison to other SNe II. Also, the former color becomes flatter during the epoch in which signatures of ejecta-CSM interaction are seen in the spectra (see Section 8.1).

The Bessell colors of SN 2016gfy were converted to SDSS colors using the transformation equations from Jordi et al. (2006) for comparison with the sample of de Jaeger et al. (2018a, hereafter DJ18a). During the late-plateau phase, DJ18a inferred that the redder SNe II display higher $H\alpha$ velocities (~ 70 days) and, steeper decline rates ($s_{2,V}$). SN 2016gfy lies outside the 3σ dispersion of the latter correlation as seen in Figure 9.

6. Spectroscopic Evolution

6.1. Early Phase (<30 days)

Figure 10 shows the early-phase spectral evolution of SN 2016gfy. The first spectrum (~ 4 days) shows narrow emission lines superposed over a blue continuum. However, the narrow features possibly owe their origin to the parent H II region as they do not cease to exist in the later epochs. No signatures of He II emission lines are seen in the very early spectra (< 5 days) of SN 2016gfy, which results from a strong progenitor wind (Khazov et al. 2016). A boxy shape of $H\alpha$ is seen in the spectrum between ~ 11 –21 days (see the discussion in Section 8.1) implying an interaction of the ejecta with the CSM (Andrews et al. 2010; Inserra et al. 2011; de Jaeger et al. 2018b).

The spectrum of ~ 11 days shows the emergence of P-Cygni Balmer features ($H\alpha$, $H\beta$, $H\gamma$, and $H\delta$) along with He I $\lambda 5876$ (which is a result of the high ejecta temperature) and the Ca II H&K doublet. The He I $\lambda 5876$ feature fades away in the spectra beyond ~ 18 days as the ejecta temperature drops with time. The signature of Fe II $\lambda 5169$ is seen in the spectrum of ~ 21 days and becomes prominent around ~ 25 days, which also marks the emergence of Fe II $\lambda\lambda 4924, 5018$. The Ba II $\lambda 4554$ blend is evident in the spectrum of ~ 21 days. It is important to note here that the emission features of $H\alpha$ and $H\beta$ are contaminated by narrow emission lines from the parent H II region throughout the evolution of the SN.

6.2. Plateau Phase

The temporal evolution of Balmer features $H\alpha$ and $H\beta$ is shown in Figure 11. The P-Cygni absorption troughs of both the features show a distinct peculiar notch (referred as “Cachito” in Gutiérrez et al. 2017) starting at ~ 33 days. The solid line in the figure depicts the evolution of the normal velocity component (NC), which follows a power-law decline trend in velocities. However, the dashed line depicts a slow temporal evolution (1000 km s^{-1} decline in ~ 80 days) of the “Cachito,” which could either be Si II 6355 \AA or a high-velocity (HV) feature of hydrogen (Gutiérrez et al. 2017). The presence of a $H\beta$ counterpart to the $H\alpha$ “Cachito” at a similar velocity

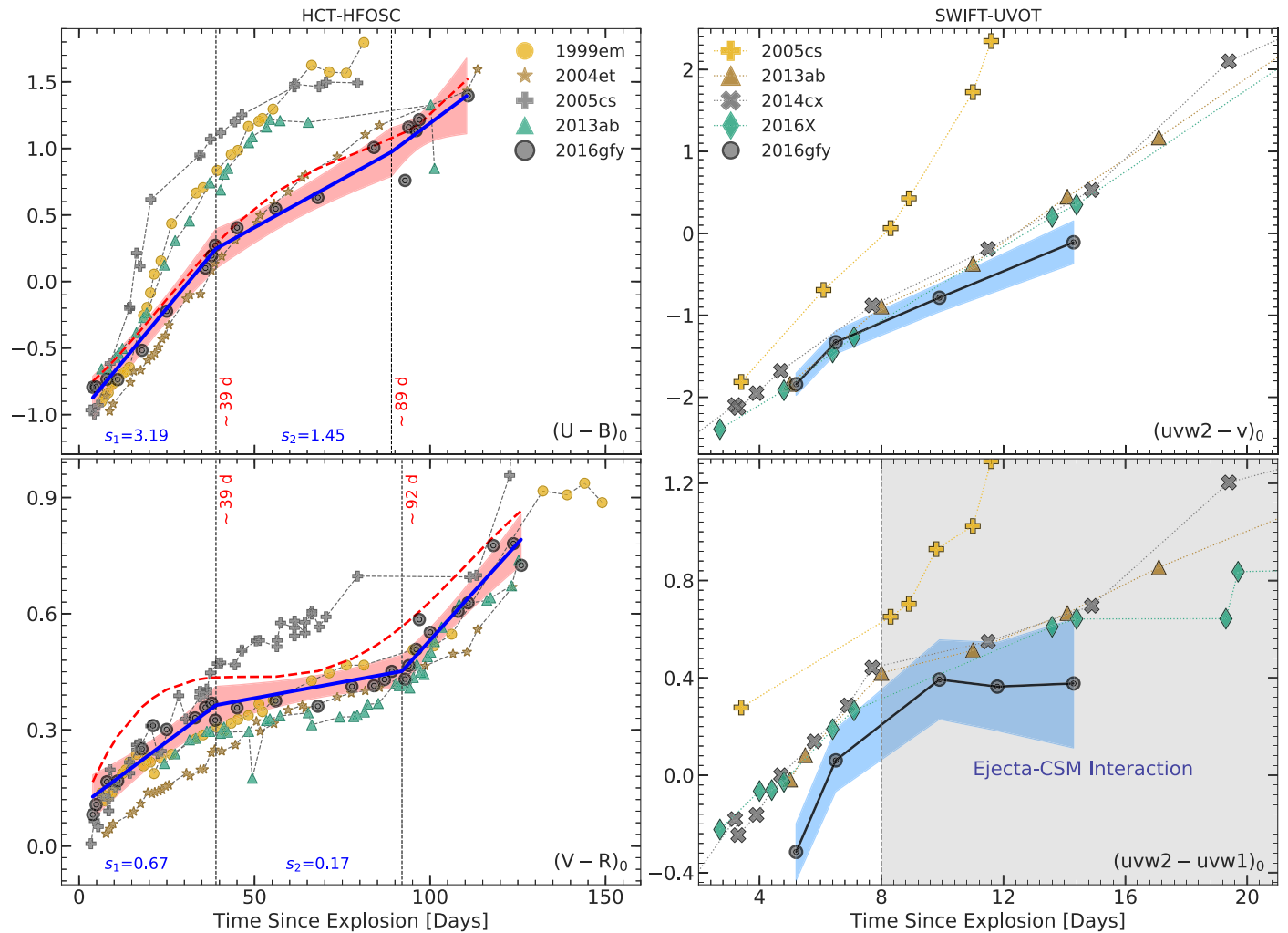


Figure 8. Intrinsic color evolution of SN 2016gfy in comparison with other SNe II. The fit to the $U - B$ and $V - R$ colors with a linear piece-wise polynomial is shown with a solid blue line and the slopes, s_1 and s_2 (see de Jaeger et al. 2018a, hereafter DJ18a), inferred from the fit are indicated in blue. Dashed vertical lines mark the epoch of transition in decline rates and 3σ confidence interval of the fits are shaded in pink. The fits to the Galactic extinction corrected color with the Legendre polynomial are shown in red. The 1σ uncertainty for the SWIFT colors are shaded in light blue.

($\sim 9500 \text{ km s}^{-1}$) strengthens its presence as an HV feature of hydrogen.

Theoretical investigation in Chugai et al. (2007) argued that the enhanced excitation of the outer ejecta can result in a “Cachito” near $H\alpha$, but they denied the presence of a $H\beta$ “Cachito” due to its low optical depth. This is in contrast with 63% of the SNe II in the sample study of Gutiérrez et al. (2017) that displayed “Cachito” near both the Balmer features. However, Chugai et al. (2007) also suggested that the “Cachito” can form behind the reverse shock, in the cold dense shell (CDS). This advocates that the HV features were produced from the interaction of the ejecta with the RSG wind (see Section 8.1).

The Fe II $\lambda\lambda 4924, 5018, 5169$ triplet strengthens as the photosphere of the SN traverses deep inside the ejecta. A weak imprint of Na I D from the SN appears in the spectrum of ~ 39 days and becomes clearly discernible in the spectrum of ~ 50 days as seen in Figure 12. The metal features of Fe II $\lambda\lambda 5267, 5363$, Sc II $\lambda 5663$ multiplet, Ba I $\lambda 6142$, and Sc II $\lambda 6246$ can be clearly sighted in the spectra past ~ 50 days. O I $\lambda 7774$ is seen during the plateau phase but becomes increasingly fainter as the SN enters the transition phase. A hint

of [O I] $\lambda\lambda 6300, 6364$ and [Ca II] $\lambda\lambda 7291, 7324$ can be spotted in the transition phase spectrum (~ 111 days).

6.3. Nebular Phase (>115 days)

The nebular phase of an SN unmasks the progenitor structure as the outer ejecta becomes optically thin. The low-resolution spectra of SN 2016gfy from HCT during this phase are shown in Figure 13 and the medium-resolution spectra from MMT in Figure 14. The spectrum of ~ 118 days depicts a flat continuum and emission-dominated spectral features of Na I D, [O I] $\lambda\lambda 6300, 6364$, $H\alpha$, [Ca II] $\lambda\lambda 7291, 7324$ and the Ca II $\lambda\lambda 8498, 8542, 8662$ NIR triplet.

The width of narrow $H\alpha$ from the parent H II region present in our medium-resolution spectra taken with MMT at $\sim 119, 175,$ and 253 days shows no indication of broadening and stays at the resolution of the instrument $\sim 2 \text{ \AA}$ (see Figure 14). This strengthens the proposition that the emission is purely from the host H II region and shows no definitive signature of CSM interaction during this phase in SN 2016gfy. Furthermore, the broad $H\alpha$ feature in the spectrum of ~ 253 days is symmetric and does not show any peculiarity. However, this does not indicate an absence of CSM (see Section 8.1).

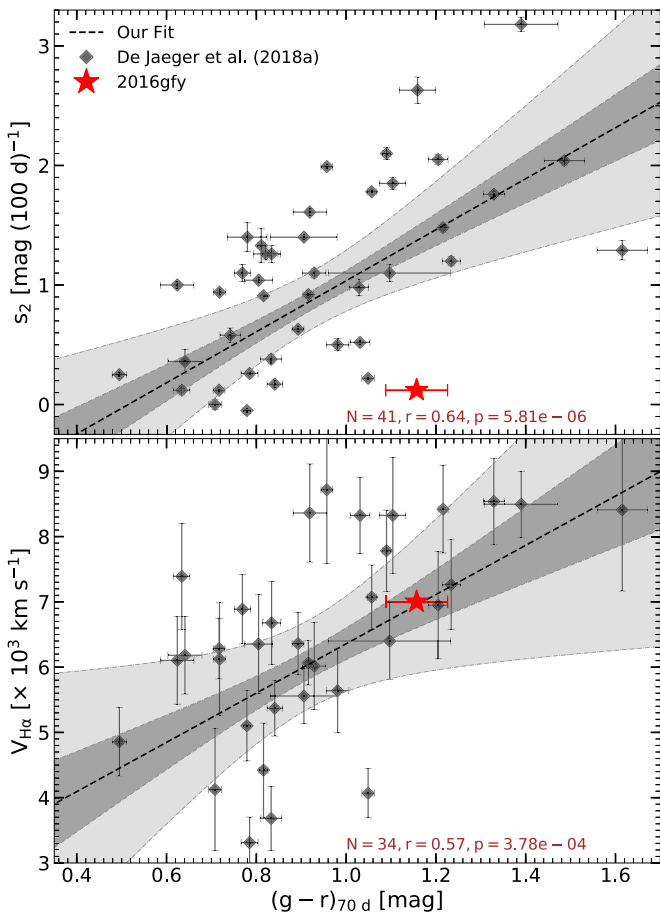


Figure 9. Correlation of $s_{2,(B-V)}$ and $H\alpha$ velocity at 70 days with $(g-r)_{70 \text{ days}}$ indicated by DJ18a. 1σ and 3σ confidence intervals of the fits are shaded in dark gray and light gray, respectively.

7. Physical Parameters of SN 2016gfy

7.1. Ejected ^{56}Ni Mass

Radioactive ^{56}Ni is produced in the explosive nucleosynthesis of Si and O in CCSNe (Arnett 1980). The radioactive decay of $^{56}\text{Ni} \rightarrow ^{56}\text{Co} \rightarrow ^{56}\text{Fe}$ thermalizes the SN ejecta and powers the late-phase (nebular) LC in SNe II through the emission of γ -rays and positrons. The ejected ^{56}Ni mass for SN 2016gfy is estimated in the ensuing subsections.

7.1.1. Estimate from the Tail Bolometric Luminosity

Hamuy (2003), in his study of 24 SNe II-P postulated a relation between the nebular-phase bolometric luminosity and the nickel mass synthesized in the explosion assuming that the γ -rays released in the radioactive decay completely thermalizes the SN ejecta. The mean tail luminosity, L_t of SN 2016gfy computed over 4 epochs (~ 199 – 241 days) with a mean phase of ~ 223 days is $5.6 \pm 1.0 \times 10^{40} \text{ erg s}^{-1}$ and yields a ^{56}Ni mass of $0.031 \pm 0.006 M_{\odot}$.

7.1.2. Comparison with SN 1987A LC

^{56}Ni mass can also be procured from the fact that highly energetic explosions yield more ^{56}Ni (Hamuy 2003) under the assumption that the γ -ray deposition is similar for the SNe in comparison. Turatto et al. (1998) obtained a ^{56}Ni mass estimate of $0.075 \pm 0.005 M_{\odot}$ for SN 1987A. A ^{56}Ni mass of

$0.033 \pm 0.008 M_{\odot}$ is estimated after comparing its bolometric luminosity with SN 1987A at ~ 241 days.

7.1.3. Fitting Late-phase LC

In Section 5, a decline rate marginally higher ($\sim 1.00 \text{ mag (100 day)}^{-1}$) than the radioactive decay rate of ^{56}Co (i.e., $0.98 \text{ mag (100 day)}^{-1}$) with complete γ -ray trapping, was determined from the V-band LC of SN 2016gfy. To account for the γ -ray leakage, Equation (3) from (Yuan et al. 2016) was fit to the late-phase LC beyond 140 days, where t_c is the characteristic timescale for the optical depth of γ -rays to become one. A ^{56}Ni mass of $0.031 \pm 0.006 M_{\odot}$ and a t_c of ~ 486 days was obtained for SN 2016gfy. The high value of t_c here is similar to that of SN 1987A (~ 530 days) and signifies insignificant γ -ray leakage in SN 2016gfy.

7.1.4. Correlation with “Steepness Parameter”

An empirical relation between the V-band decline rate during the transitional phase (“steepness parameter,” $S = -dM_V/dt$) and the ejected ^{56}Ni mass was reported by Elmhamdi et al. (2003a) using 10 SNe II, which was later improved upon in Singh et al. (2018) using a sample of 39 SNe II. A steepness parameter of 0.121 was determined for SN 2016gfy using its V-band LC, which yields a ^{56}Ni mass of $0.036 \pm 0.004 M_{\odot}$ using the relation from Singh et al. (2018).

The slightly higher ^{56}Ni mass estimate obtained using the steepness parameter in comparison with other techniques is an indication that the LC of SN 2016gfy exhibits a non-negligible degree of ^{56}Ni -mixing, which can decrease the steepness during the transition phase (Kozyreva et al. 2019).

7.1.5. Mean Estimate of ^{56}Ni Mass

All the above methods return a mean ejected ^{56}Ni mass of $0.033 \pm 0.003 M_{\odot}$ for SN 2016gfy. The use of the pseudo-bolometric ($UBVRI$) LC in determining the ^{56}Ni mass, makes the inferred estimate a lower limit for the ^{56}Ni synthesized in SN 2016gfy.

7.2. Ejecta Velocity

Progenitors of CCSNe have an “onion-ring” structure of elements, whose spectral features show up at varied velocities in an SN as they originate at different heights (and times). The line velocities were inferred from the blueshifted minima of the P-Cygni absorption profiles in the redshift corrected spectra. The velocity evolution of $H\alpha$, $H\beta$, $H\gamma$, He I $\lambda 5876$, Fe II $\lambda\lambda 4924$, 5018 , and 5169 is shown in Figure 15. The Balmer lines show faster velocities as their integrated extent of line formation has a higher radii than the radius of the photosphere (optical depth $\sim 2/3$, Leonard et al. 2002b). During the plateau phase, the velocities computed from the Fe II acts as a good proxy for the photospheric velocity (Dessart & Hillier 2005).

The line velocity in SNe II is known to decrease as a power law (Hamuy et al. 2001). A power-law fit returned exponents of -0.291 ± 0.010 and -0.641 ± 0.018 for the $H\alpha$ and Fe II $\lambda 5169$ features in SN 2016gfy, respectively. The comparison of line velocity evolution of SN 2016gfy with other SNe II along with the power-law fits is shown in Figure 16. The $H\alpha$ velocity evolution matches the bright Type II SN 2013ej (Bose et al. 2015a) and stays faster compared to other SNe II. The Fe II $\lambda 5169$ evolution is similar to the average value derived

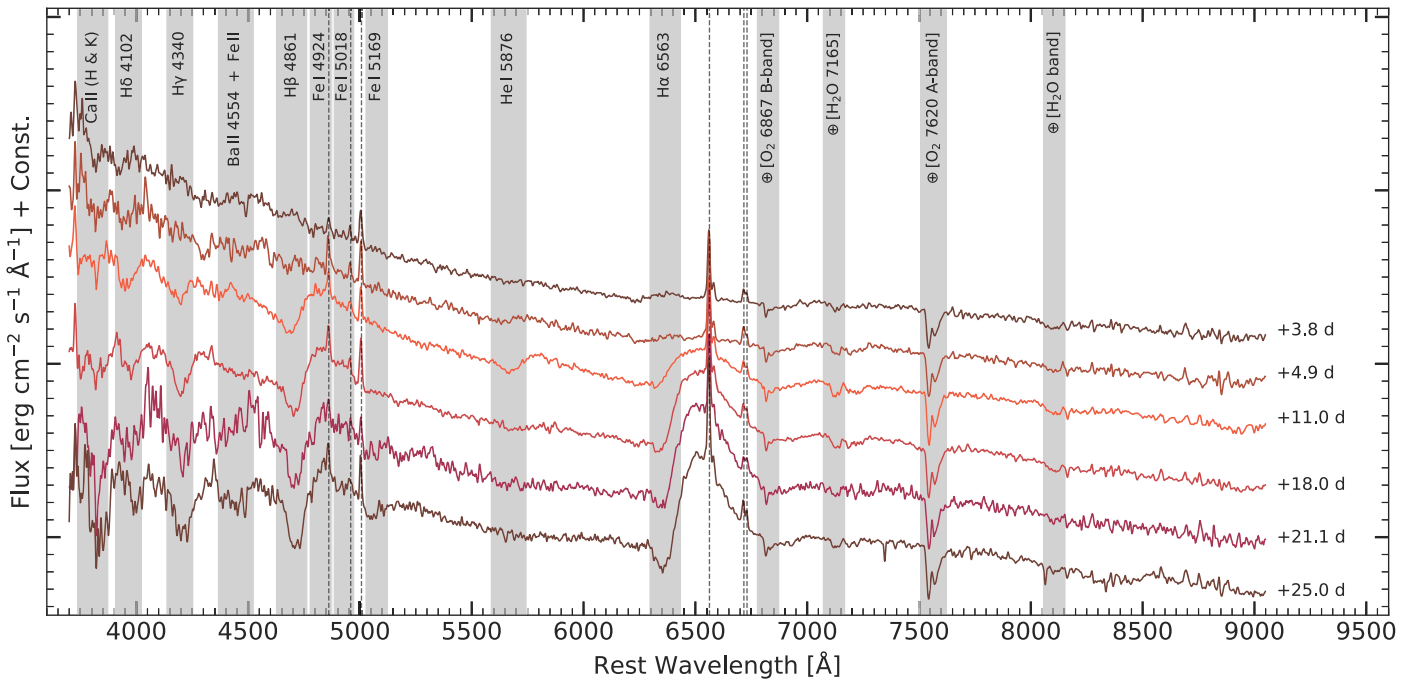


Figure 10. Early phase (<30 days) spectra of SN 2016gfy from HCT-HFOSC. The spectra are corrected for the redshift of the host galaxy. Prominent emission lines of H β 4861 Å, [O III] 4959 Å, [O III] 5007 Å, H α 6563 Å, [N II] 6584 Å, and [S II] 6717, 6731 Å from the parent H II region are marked with dashed vertical lines. The HCT-HFOSC spectra shown in Figures 10 through 13 are available as data behind the figure.

(The data used to create this figure are available.)

from samples of SNe II-P (-0.581 ± 0.034) in Faran et al. (2014b) and SNe II (-0.55 ± 0.20) in de Jaeger et al. (2015). In the case of SN 2016gfy, the velocities measured during the mid-plateau phase (~ 50 days) are $\sim 7900 \text{ km s}^{-1}$ and $\sim 4150 \text{ km s}^{-1}$ for H α and Fe II $\lambda 5169$, respectively. This is faster than the mean values of ~ 6500 and $\sim 3500 \text{ km s}^{-1}$ inferred for SNe II from the sample of Gutiérrez et al. (2017).

7.3. Temperature and Radius Evolution

The evolution of the observed color temperature (T_c) of SN 2016gfy is estimated with a blackbody fit to spectral energy distribution (SED) constructed using the extinction corrected *UBVRI* fluxes and is shown in Figure 17. The radius is estimated from the Stefan–Boltzmann law for a spherical blackbody, i.e., $R = (L/4\pi\sigma T^4)^{0.5}$. The temperature drops swiftly in the first 40 days and is ascribable to the rapid cooling of the expanding envelope. Also plotted is the radius of the line-forming region estimated from the velocity evolution of the Fe II $\lambda 5169$ feature. This radius is similar to the photospheric radii in SNe II inferred from the blackbody fits to the SED within an order of magnitude (Dessart & Hillier 2005; Arcavi et al. 2017), as is seen in the case of SN 2016gfy.

7.4. Progenitor Properties

To understand the relation of the observable parameters to the progenitor properties, (Litvinova & Nadezhin 1985, hereafter LN85) performed hydrodynamical modeling on a grid of SNe II. Using their empirical relations with a plateau length of $t_p = 90 \pm 5$ days, a mid-plateau photospheric velocity of $v_{\text{ph}} = 4272 \pm 53 \text{ km s}^{-1}$, a mid-plateau *V*-band absolute magnitude of $M_V^{50} = -16.74 \pm 0.22$ mag, a progenitor radius of $310 \pm 70 R_\odot$, an explosion energy of 0.90 ± 0.15

foe (1 foe = 10^{51} erg), and an ejecta mass of $13.2 \pm 1.2 M_\odot$ is inferred for SN 2016gfy.

Approximate physical properties of SNe II and the progenitor parameters can also be obtained from the semi-analytical formulation of Nagy et al. (2014). Their revised two-component framework (Nagy & Vinkó 2016, hereafter N16) comprising of a dense inner core with an extended massive outer envelope was used to model the LC of SN 2016gfy. The late-plateau bump in SN 2016gfy was not reproduced by the two-component fit (see Figure 7). However, the early plateau phase, transition phase, and nebular phase were reproduced well. A radius of $\sim 350 R_\odot$, an ejecta mass of $11.5 M_\odot$, and an explosion energy of 1.4 foe were estimated for SN 2016gfy from the best fit.

Using the characteristic timescale t_c , estimated in Section 7.1.3, a uniform density profile, γ -ray opacity of $0.033 \text{ cm}^2 \text{ g}^{-1}$ and a kinetic energy of 0.9 foe (from LN85) for the ejecta, an ejecta mass of $\sim 13.0 M_\odot$ is inferred for SN 2016gfy utilizing the diffusion equation from Terreran et al. (2016, Equation (3)).

The mass of the progenitor was also constrained using the nebular phase spectra (>150 days) as the SN ejecta becomes transparent, revealing the dense inner core. The intensities of prominent emission lines during this phase help constrain the elemental abundances and hence indicate the ZAMS mass of the progenitor (Jerkstrand et al. 2014, hereafter J14). The [Ca II]/[O I] flux ratio in the late nebular phase (>200 days) remains constant because the mass of calcium produced in the explosion is insensitive to the progenitor mass whereas the oxygen mass depends on it (Fransson & Chevalier 1989). A higher-mass progenitor has a stronger [O I] $\lambda\lambda 6300, 6364$ feature in comparison with H α and [Ca II] $\lambda\lambda 7291, 7324$. Hence, the [Ca II]/[O I] flux ratio of ~ 1.2 in the spectrum of

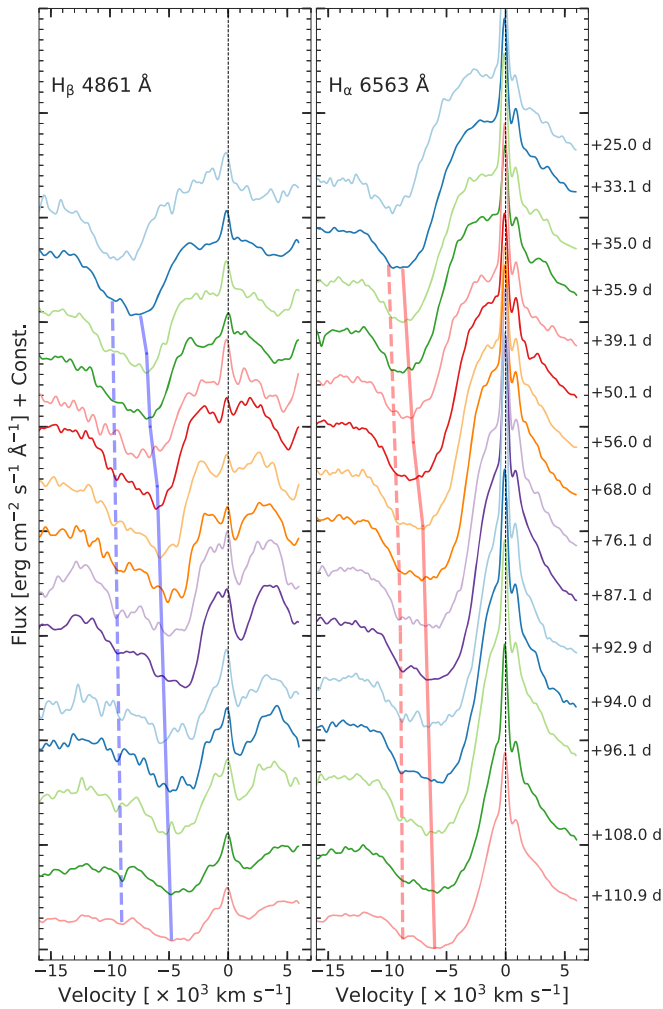


Figure 11. Temporal evolution of the Balmer features, $H\alpha$ and $H\beta$ in SN 2016gfy. The solid lines depict the evolution of the normal velocity component whereas the dashed lines show the evolution of the high-velocity features. The HCT-HFOSC spectra shown in Figures 10 through 13 are available as data behind Figure 10.

~ 216 days indicates a low-mass progenitor of SN 2016gfy (Maguire et al. 2010; Sahu et al. 2013).

Also, the strength of the [O I] $\lambda\lambda 6300, 6364$ emission feature in the nebular phase is relatively insensitive to the explosive nucleosynthesis in an SN and exhibits the progenitor’s oxygen abundance, which tightly correlates with the M_{ZAMS} of the progenitor (Woosley & Weaver 1995). In order to perform an accurate comparison, the modeled spectra from J14 were scaled to the estimated distance (see Appendix B) and the amount of ^{56}Ni synthesized (see Section 7.1) for SN 2016gfy. The spectra were also corrected for differences in γ -ray leakage across the models and our spectrum using the following equation:

$$F_{\text{obs}} = F_{\text{decay}} * (1 - e^{-t_c^2/t^2}), \quad (2)$$

where t_c is the characteristic timescale (see Section 7.1.3), F_{decay} is the flux from the radioactive decay, and F_{obs} is the observed flux. However, phase correction was not applied as the observed and the synthetic spectrum were only separated by ~ 4 days. The modeled nebular spectra from J14 for progenitors of masses 12, 15, 19, and $25 M_{\odot}$ are compared with the ~ 216 day spectrum of SN 2016gfy in Figure 18. The [O I] doublet of SN 2016gfy

matches closely to the J14 model of $15 M_{\odot}$ and is backed by the findings of S16, who showed that models with a M_{ZAMS} below $12.5 M_{\odot}$ are inefficient at producing oxygen.

The net amount of oxygen varies from 0.2 to $5 M_{\odot}$ for CCSNe progenitors in the mass range of 10 – $30 M_{\odot}$ (Woosley & Heger 2007). During the late nebular phase (>200 days), the luminosity of the [O I] doublet is powered by γ -ray deposition in the oxygen content of the SN, and hence correlates with the oxygen mass (Elmhamdi et al. 2003b). Using an [O I] flux of $7.81 \times 10^{-15} \text{ erg s}^{-1}$ in the spectrum of ~ 216 days for SN 2016gfy and an oxygen mass of 1.2 – $1.5 M_{\odot}$ for SN 1987A (Chugai 1994), an oxygen mass of 0.8 – $1.0 M_{\odot}$ is inferred for SN 2016gfy, assuming similarity with SN 1987A in the efficiency of energy deposition and the excited mass.

Morozova et al. (2016) modeled the early-phase LCs of SNe II using the SuperNova Explosion Code (SNEC; Morozova et al. 2015) and showed that the rise-time depends on the progenitor radii. Using their relation between the progenitor radius at the time of explosion and the V -band rise time (instead of g -band in their work) of 9.07 ± 0.36 days, a progenitor radius of $733 \pm 36 R_{\odot}$ is estimated for SN 2016gfy. However, due to the effect of CSM on the early LC (and the rise time) of SN 2016gfy, the above technique may not truly reflect the progenitor radius. The progenitor parameters estimated for SN 2016gfy using various techniques are summarized in Table 4.

The effect of progenitor metallicity on the spectra of SNe II was first indicated in the theoretical modeling of SN atmospheres (D14). This conjecture was further strengthened in the study of A16, who provided observational evidence for the correlation between the metallicity of the host H II region and the pseudo-equivalent widths (pEW) of metal lines during the photospheric phase (plateau) of SNe II. The pEW was measured from a Gaussian fit after defining a pseudo-continuum on either side of the absorption feature. In order to determine the progenitor metallicity of SN 2016gfy, the pEW of Fe II $\lambda 5169$ feature was measured in the plateau phase and was compared with the $15 M_{\odot}$ progenitor models (D13) of different metallicities ($0.1, 0.4, 1.0, 2.0 Z_{\odot}$) in Figure 19.

The estimated pEW for SN 2016gfy lies between the 0.1 and $0.4 Z_{\odot}$ models of D13 and is consistent with the weak presence of [Ca II] $\lambda\lambda 7291, 7324$ during the plateau phase, indicating a low progenitor metallicity. This can also possibly explain the disappearance of Ca II NIR triplet in the nebular spectra due to its low abundance in the progenitor. This result is in coherence with the subsolar oxygen abundance estimated for the parent H II region in Section 3.3. It should be noted here that the mixing-length (mlt) parameter in the theoretical models could significantly alter the pEWs of metal lines as a result of differences in the progenitor radii along with the fact that D13 models are not tailored for the progenitor of SN 2016gfy.

8. Discussion

8.1. Early-phase CSM–Ejecta Interaction

The boxy emission profile of $H\alpha$ seen in the spectra of SN 2016gfy during ~ 11 – 21 days is an indication of interaction between the fast-moving SN shock and the slow-moving shell-shaped CSM (Chevalier & Fransson 1994; Morozova et al. 2017). Figure 20 shows the evolution of the boxy features in SN 2016gfy in the top panel, with a comparison to other SNe II that show similar features in the middle panel and those that do not in the bottom panel. Narrow Balmer emission lines are also

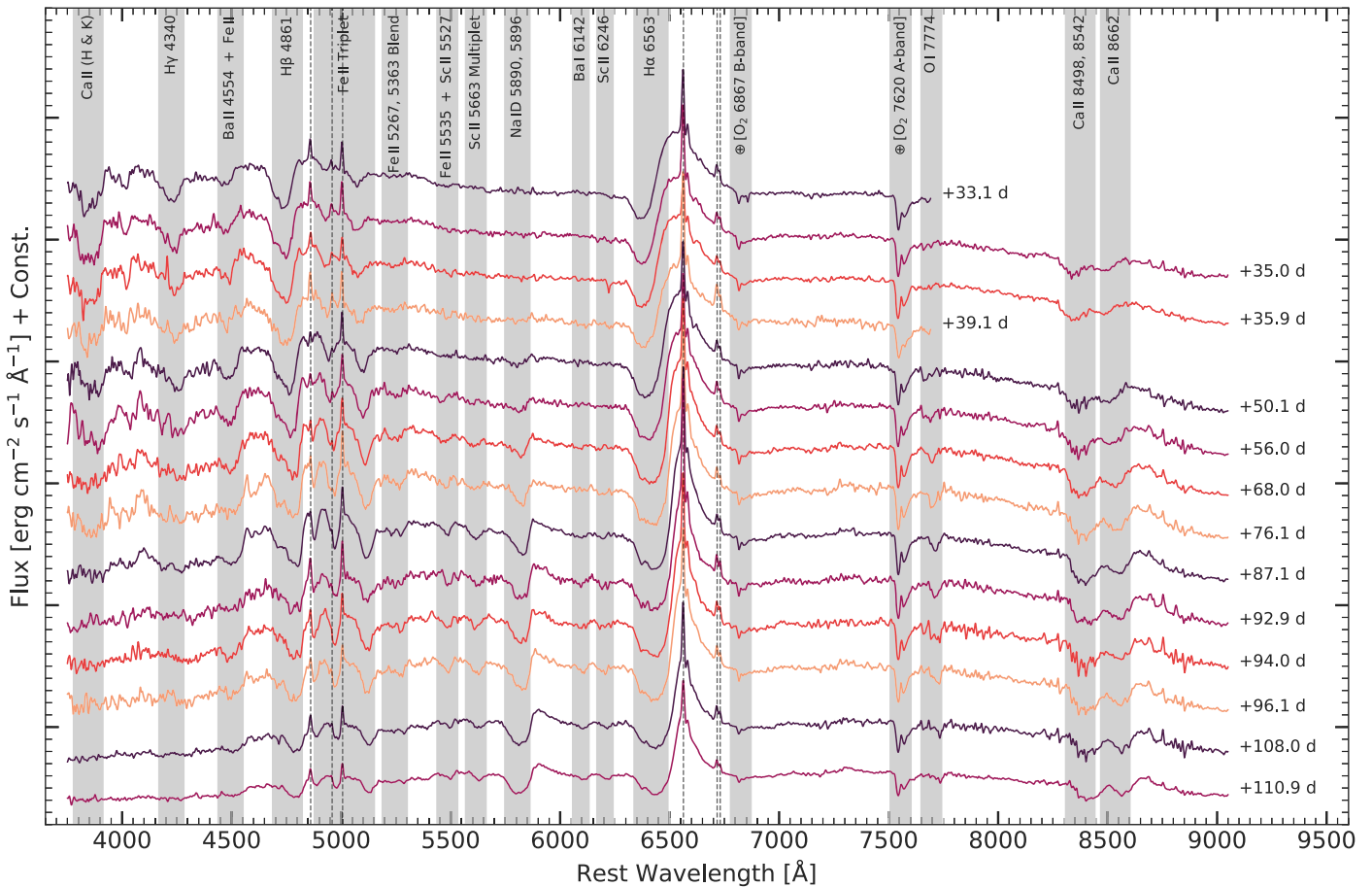


Figure 12. Plateau and transition phase (<115 days) spectra of SN 2016gfy from HCT-HFOSC. The plot description is the same as that of Figure 10. The HCT-HFOSC spectra shown in Figures 10 through 13 are available as data behind Figure 10.

seen in the case of an interaction with a massive CSM shell (Nakaoka et al. 2018). However, the contamination from narrow features of the parent H II region in the spectra of SN 2016gfy makes it difficult to isolate such signatures.

The boxy profile is not seen in the spectrum of ~ 5 days and fades away past the spectrum of ~ 25 days in the case of SN 2016gfy, giving an estimated length of interaction with the CSM as 17 ± 3 days (epoch of interaction ~ 8 –25 days). Using an ejecta velocity of $\sim 13,000 \text{ km s}^{-1}$ on day 8 (see Figure 15), the inner radius of the CSM is estimated as ~ 60 au. The duration of interaction coupled with the average $H\alpha$ velocity during the period ($\sim 10,000 \text{ km s}^{-1}$) gives a thickness of 110 au for the CSM shell. Assuming a wind velocity of 10 km s^{-1} (Smith 2014, for an RSG), the progenitor of SN 2016gfy experienced an episode of enhanced mass loss 30–80 yr preceding the explosion.

The interaction of the ejecta with the slowly moving CSM is seen in the spectra of SN 2016gfy beyond ~ 25 days in the form of HV features of $H\alpha$ and $H\beta$, which evolve slowly throughout the spectra (9500 – 8500 km s^{-1} in a period of ~ 80 days). This is similar to the case of SN 2013ej where weak CSM interaction was inferred in the early phase (Bose et al. 2015a; Das & Ray 2017). The broad emission lines of $H\alpha$ and [O I] $\lambda\lambda 6300, 6364$ seen in the late-phase optical spectra of Type II SN 1980K (Chevalier & Fransson 1994) and SN 2007od (Inserra et al. 2011) also signify CSM interaction. However, no such features are seen in the late-phase spectra of

SN 2016gfy, possibly due to the absence of CSM at that distance and/or low signal-to-noise ratio (SNR) of the spectra.

As presented in previous studies, not only SN spectra but also early LCs are likely affected by the dense CSM (e.g., Moriya et al. 2017, 2018; Morozova et al. 2017; Forster et al. 2018). This interaction converts the kinetic energy of the ejecta upon collision with the nearby CSM into radiative energy and boosts up the early-phase luminosity of SN 2016gfy. It was shown in the previous section that the early bolometric LC of SN 2016gfy has the “shell” component, which likely originates from the CSM interaction (N16). To estimate the amount of the dense CSM required to explain the early LC bump, numerical LC modeling of the interaction between the SN ejecta and the dense CSM was performed. The method adopted is similar to that of Moriya et al. (2018) and we refer the reader to their study for the complete details of the numerical modeling.

Briefly, the radiation hydrodynamics code STELLA (Blinnikov et al. 1998, 2000, 2006) is used. The progenitor model of $10 M_{\odot}$ at ZAMS and solar metallicity from S16 is used (see Figure 21). The mass cut is set at $1.4 M_{\odot}$ and the explosion is triggered by putting thermal energy just above the mass cut. The explosion energy is 10^{51} erg and the ^{56}Ni mass is $0.055 M_{\odot}$ in the given model. A dense CSM with a mass-loss rate of $10^{-3} M_{\odot} \text{ yr}^{-1}$ and the terminal wind velocity of 10 km s^{-1} is put taking wind acceleration into account with the wind acceleration parameter, $\beta = 2.5$ in determining the CSM density structure (Moriya et al. 2017). High-mass loss rate here can be explained by wave-driven mass loss (Quataert &

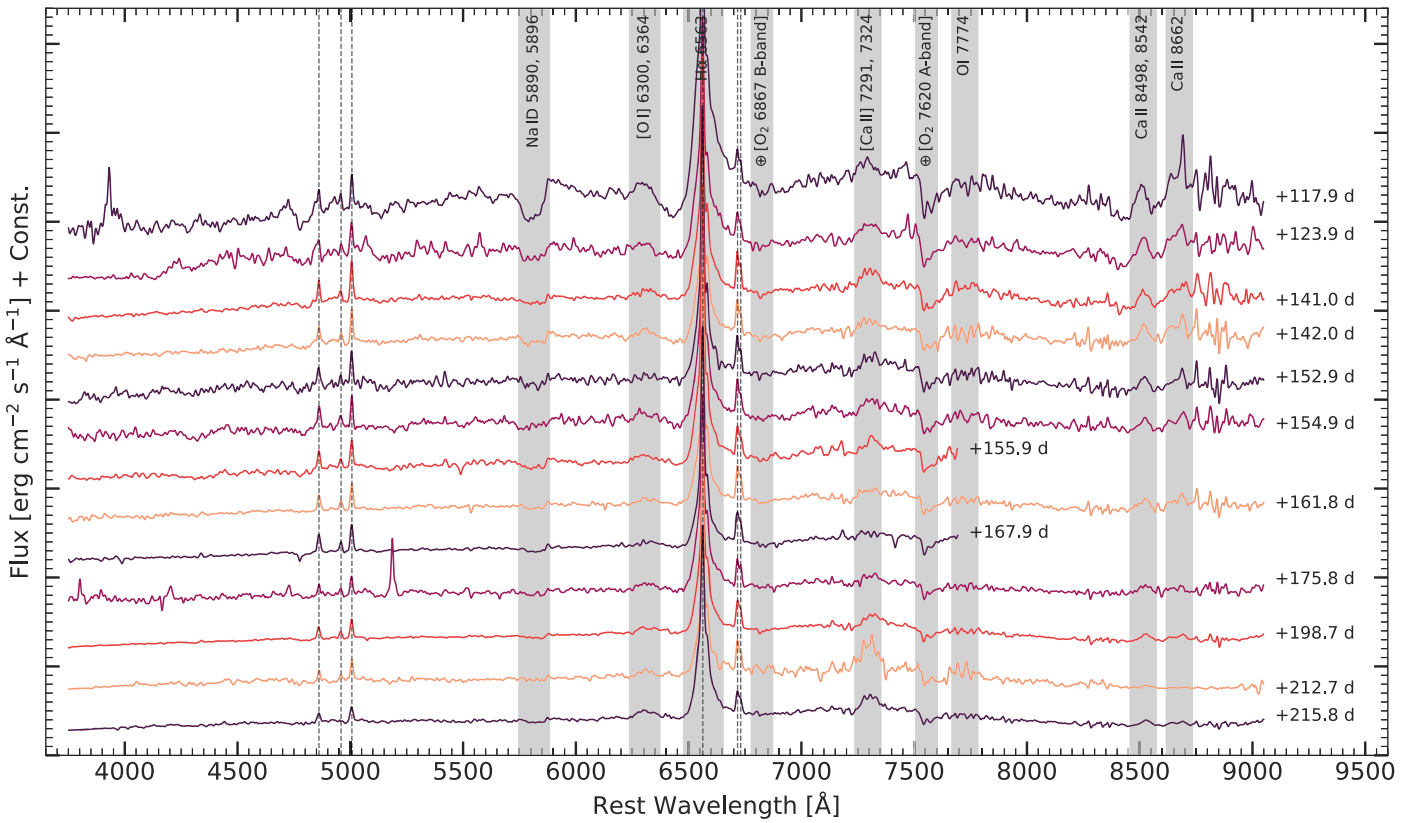


Figure 13. Nebular phase (>115 days) spectra of SN 2016gfy from HCT-HFOSC. The spectra are emission dominated with a flat continuum. The plot description is the same as that of Figure 10. The HCT-HFOSC spectra shown in Figures 10 through 13 are available as data behind Figure 10.

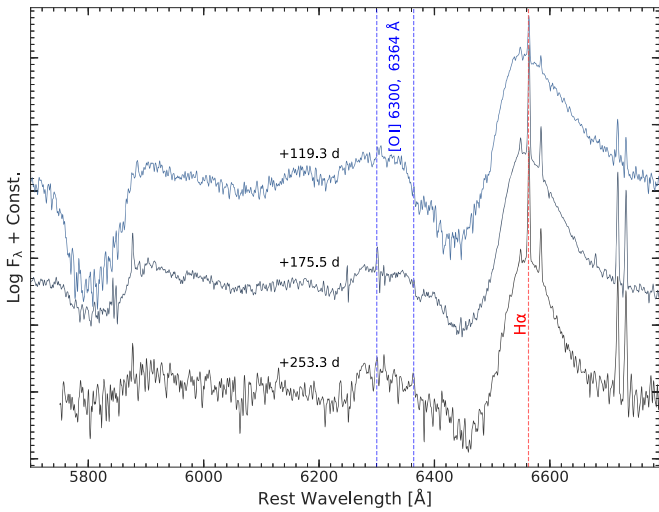


Figure 14. Medium-resolution nebular spectra of SN 2016gfy from the BC spectrograph mounted on the 6.5 m MMT. The rest-wavelengths of H α and [O I] doublet are indicated with dashed lines. The MMT spectra are available as data behind the figure.

(The data used to create this figure are available.)

Shiode 2012). The dense CSM is extended to 10^{15} cm (~ 70 au) with a total mass of $0.15 M_{\odot}$. These CSM parameters are often found in SNe II (Forster et al. 2018).

A late-plateau bump (besides the early bump) is prominently seen in the *VRI* LCs of SN 2016gfy, which could emerge from an extended interaction with the CSM. This interaction may

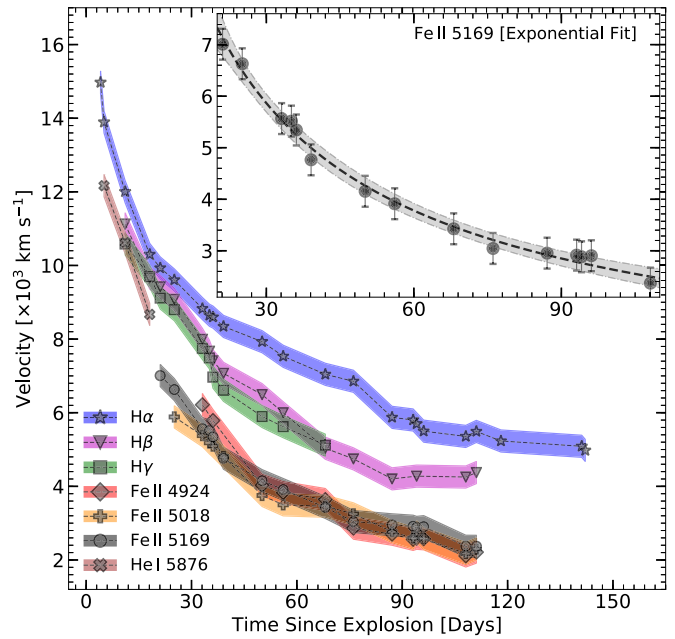


Figure 15. Line velocity evolution of spectral features in SN 2016gfy: H α , H β , H γ , He I 5876 Å, and the Fe II triplet. The velocities were determined from the blueshifted absorption minima of the P-Cygni profile.

result in the presence of narrow Balmer features, the signature of which is not seen in our spectral sequence during this phase. However, the narrow lines from the interaction can be enveloped by the SN photosphere as in the case of PTF11iqb (Smith et al. 2015) and iPTF14hls (Andrews & Smith 2018).

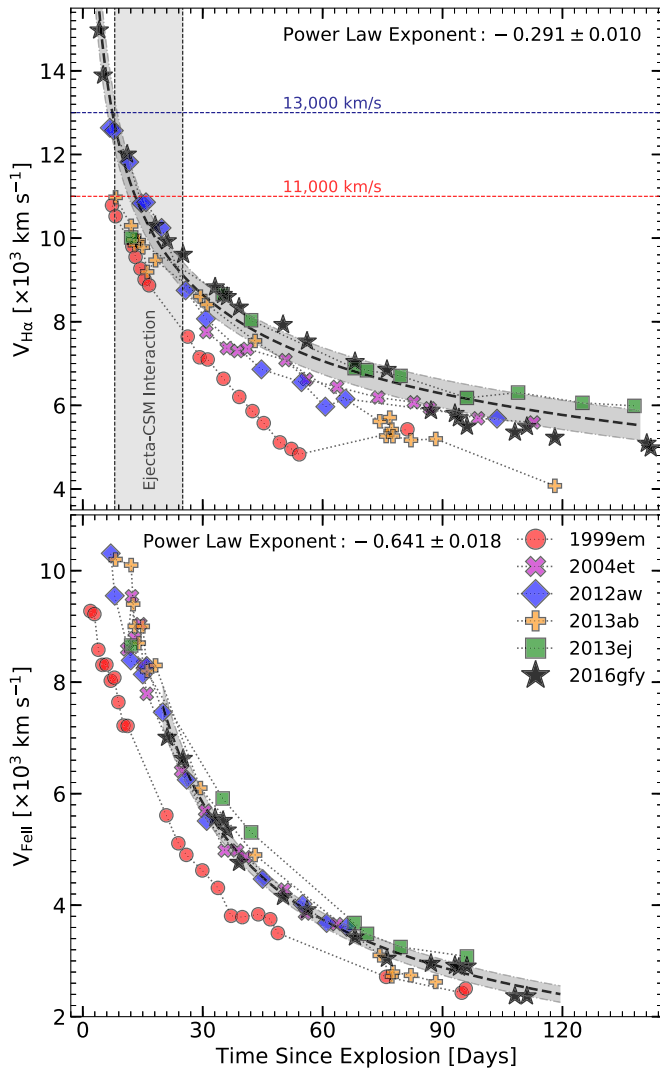


Figure 16. Comparison of line velocity evolution of SN 2016gfy with SNe II from the literature. Top and bottom panel displays the velocity evolution of H α and Fe II λ 5169, respectively. The data adopted for comparison are from Bose & Kumar (2014) and references therein.

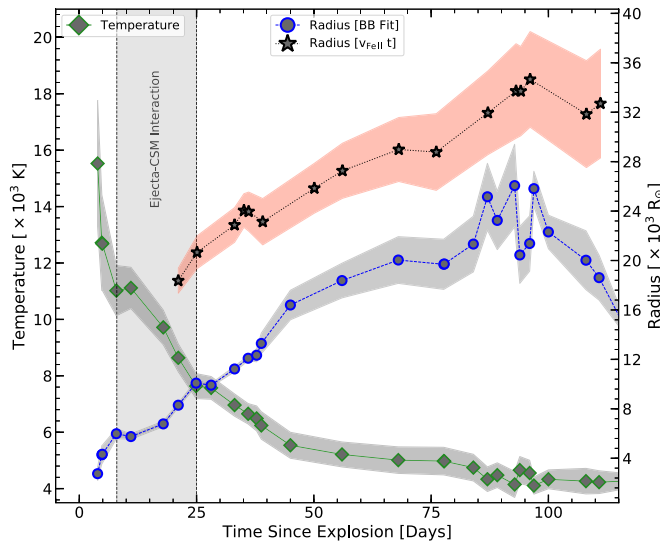


Figure 17. Temperature evolution of SN 2016gfy estimated from blackbody fits to the *UBVR* fluxes. Radius is calculated using Stefan–Boltzmann law ($R = \sqrt{L/4\pi\sigma T^4}$).

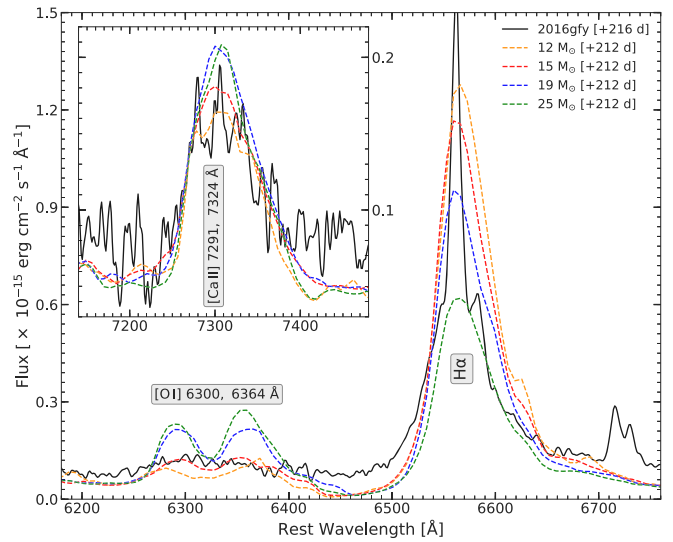


Figure 18. Comparison of the nebular spectra (~ 216 days) of SN 2016gfy with synthetic spectra from Jerkstrand et al. (2014) at ~ 212 days past the explosion.

This scenario cannot be ruled out for SN 2016gfy due to the lack of very late-phase data, in which the photosphere would have receded enough to reveal the hidden CSM–ejecta interaction region. Hence, CSM interaction is a plausible source of luminosity during this phase.

Nakar et al. (2016) explored the effect of ^{56}Ni -mixing in the ejecta of SNe II and showed that such mixing can alter the plateau duration and/or the decline rate. We therefore, explore ^{56}Ni -mixing as an alternate mechanism to explain the late-plateau bump.

8.2. Case of Ni-mixing in the Late-Plateau?

Radioactivity does not extensively alter the plateau phase luminosity due to the long diffusion time in comparison with the recombination time (KW09). This is, however, untrue for Type II-P/L SNe that have a progenitor smaller (in radius) than an RSG (e.g., Blue Super Giant in case of SN 1987A) or synthesize a large amount of ^{56}Ni ($>0.1 M_{\odot}$). However, the plateau is lengthened in proportion to the ^{56}Ni synthesized as the energy from the radioactive decay keeps the ejecta gas ionized longer (S16). SN 2016gfy shows a bump in the late-plateau phase (~ 50 – 95 days, see Figure 5), which is not seen in a majority of bright SNe II (< -17.0 mag).

LCs of SNe II past the photospheric phase show a significant drop to the radioactive tail. The contribution from the cooling envelope becomes negligible relative to the radioactive decay chain ($^{56}\text{Ni} \rightarrow ^{56}\text{Co} \rightarrow ^{56}\text{Fe}$) past the luminosity drop at the end of the transition phase, t_{Ni} . The fleeting deposition of energy into the ejecta as a result of the ^{56}Ni decay (Nakar et al. 2016) is given by:

$$Q_{\text{Ni}}(t) = \frac{M_{\text{Ni}}}{M_{\odot}} (6.45e^{-t/8.8} + 1.45e^{-t/111.3}) \times 10^{43} \text{ erg s}^{-1}, \quad (3)$$

where t is the time since the explosion in days and M_{Ni} is the mass of ^{56}Ni synthesized. To study the effect of ^{56}Ni on the early-phase LC, Nakar et al. (2016) defined the observable η_{Ni} to disentangle the fraction of bolometric luminosity contributed

Table 4
Progenitor Parameters Estimated for SN 2016gfy Using Various Techniques

Technique	M_{Ni} (M_{\odot})	M_{ej} (M_{\odot})	E_{k} (10^{51} erg)	Radius (R_{\odot})
Empirical relation (Litvinova & Nadezhin 1985)	...	13.2 ± 1.2	0.90 ± 0.15	310 ± 70
Two-component model (Nagy & Vinkó 2016)	0.029	~ 11.5	~ 1.4	~ 350
Diffusion relation (Terreran et al. 2016)	...	~ 13.0
Comparison of nebular spectra (Jerkstrand et al. 2014)	...	~ 15 (M_{ZAMS})
Correlation of rise-time and progenitor radii (Morozova et al. 2016)	733 ± 36

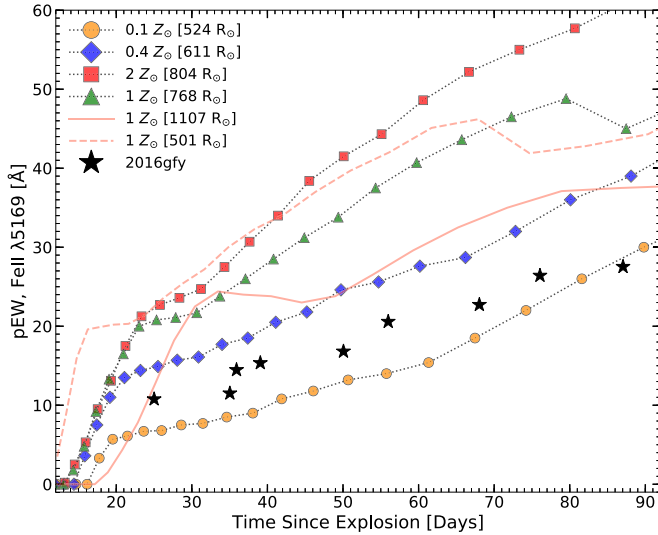


Figure 19. Temporal evolution of pEW of Fe II $\lambda 5169$ feature estimated from the observed spectra of SN 2016gfy during the plateau phase. The comparison with the theoretical models (shown with a dotted line) of a $15 M_{\odot}$ progenitor with different metallicities from D13 is also shown. The dashed and solid lines differ from the other models in the mixing length parameter.

by $Q_{\text{Ni}}(t)$ from the contribution due to the cooling envelope. The observable is defined as:

$$\eta_{\text{Ni}} = \frac{\int_0^{t_{\text{Ni}}} t Q_{\text{Ni}}(t) dt}{\int_0^{t_{\text{Ni}}} t (L_{\text{bol}}(t) - Q_{\text{Ni}}(t)) dt}, \quad (4)$$

where $L_{\text{bol}}(t)$ is the bolometric luminosity at time t . An η_{Ni} of 0.60 is obtained for SN 2016gfy, which translates to a $\sim 38\%$ contribution by ^{56}Ni decay to the time-weighted bolometric luminosity during the plateau phase. The η_{Ni} values inferred for the sample of SNe II in Nakar et al. (2016) lie within the range of 0.09–0.71 (except for SN 2009ib) and indicates a non-negligible contribution in the photospheric phase from the decay of ^{56}Ni .

^{56}Ni can either extend the plateau duration (without any change in the decline rate) and/or cause flattening of the plateau phase (lower the decline rate). A centrally concentrated ^{56}Ni is likely to lengthen the plateau because ^{56}Ni does not diffuse out until the end of the plateau phase (see Figure 4 in Kozyreva et al. 2019). If ^{56}Ni is uniformly mixed in the envelope, it increases the luminosity during the plateau phase (and flattens it) as ^{56}Ni diffuses out earlier in comparison with a centrally concentrated ^{56}Ni . The phase during which ^{56}Ni starts affecting the LC is dependent on the degree of ^{56}Ni mixing in the envelope (Kozyreva et al. 2019).

The effect of ^{56}Ni on the plateau phase is more pronounced in the case of higher ^{56}Ni mass and lower explosion energy (Kozyreva et al. 2019). The case of an extremely long plateau in

SN 2009ib (Takáts et al. 2015) is partially due to the former reasons but could only be explained with complete mixing of ^{56}Ni in the envelope as it results in a smoother plateau evolution. No observable transition (due to the dominance of ^{56}Ni) in the plateau phase is seen in such cases regardless of the value of η_{Ni} .

At the intermediate value of η_{Ni} ($=0.60$) inferred for SN 2016gfy, the emission from the cooling envelope and the ^{56}Ni decay becomes comparable during the late-plateau phase. Unlike the case of SN 2009ib, the slight bump noticed in SN 2016gfy could only be a result of centrally concentrated or partially mixed ^{56}Ni . As the bump is evident only past ~ 50 days, the theoretical LCs in Kozyreva et al. (2019) point toward a ^{56}Ni -mixing with one-third of the ejecta.

Nakar et al. (2016) defined two other dimensionless variables to quantify the effect of ^{56}Ni , given as:

$$\Lambda \equiv \frac{L_{25} \cdot (80 \text{ d})^2}{\int_0^{t_{\text{Ni}}} t L_{\text{bol}}(t) dt}, \quad \Lambda_e \equiv \frac{L_{e,25} \cdot (80 \text{ d})^2}{\int_0^{t_{\text{Ni}}} t (L_{\text{bol}}(t) - Q_{\text{Ni}}(t)) dt}, \quad (5)$$

where L_{25} and L_e are the observed and hypothetical bolometric luminosities (when no ^{56}Ni is synthesized in the explosion) on day 25, respectively. The quantities $2.5 \log_{10} \Lambda$ and $2.5 \log_{10} \Lambda_e$ are indicators of plateau decline rates in units of $\text{mag} (50 \text{ day})^{-1}$, with and without the effect of ^{56}Ni , respectively. A difference ($\Lambda - \Lambda_e$) of ~ 0.5 is estimated for SN 2016gfy, which translates to a change in slope of $\sim 1 \text{ mag} (100 \text{ day})^{-1}$ due to the effect of ^{56}Ni during the plateau phase. This explains the bump in the late-plateau phase of the bolometric LC wherein a decline is mostly seen.

This effect is similar to the transition from s_1 to s_2 seen in most SNe II (Anderson et al. 2014) but the degree of flattening varies across the sample. Brighter SNe II ($M_V < -17.0 \text{ mag}$) tend to have higher inherent luminosity (and explosion energy) and hence the effect of ^{56}Ni during the plateau is minimized, leading to steeper decline rates. However, the presence of this effect in SN 2016gfy ($M_V \sim -17.1 \text{ mag}$) signifies a lower explosion energy.

8.3. Is SN 2016gfy a Typical SN II?

The first observed spectrum of SN 2016gfy is compared with the first week spectra of SNe II from the literature in the top panel of Figure 22. SN 2016gfy shows a blue featureless continuum at this epoch, similar to the spectrum of SN 2016esw. However, this is in contrast to other SNe II that show P-Cygni Balmer features along with He II $\lambda 5876$. The bottom panel in Figure 22 shows comparison during the steeper part of the plateau phase. Here, the overall spectrum of SN 2016gfy resembles the spectra of other SNe II, with noticeable differences only in the metal line strengths. This can be attributed to the lower metallicity of the progenitor (see Section 7.4) in comparison to other SNe II.

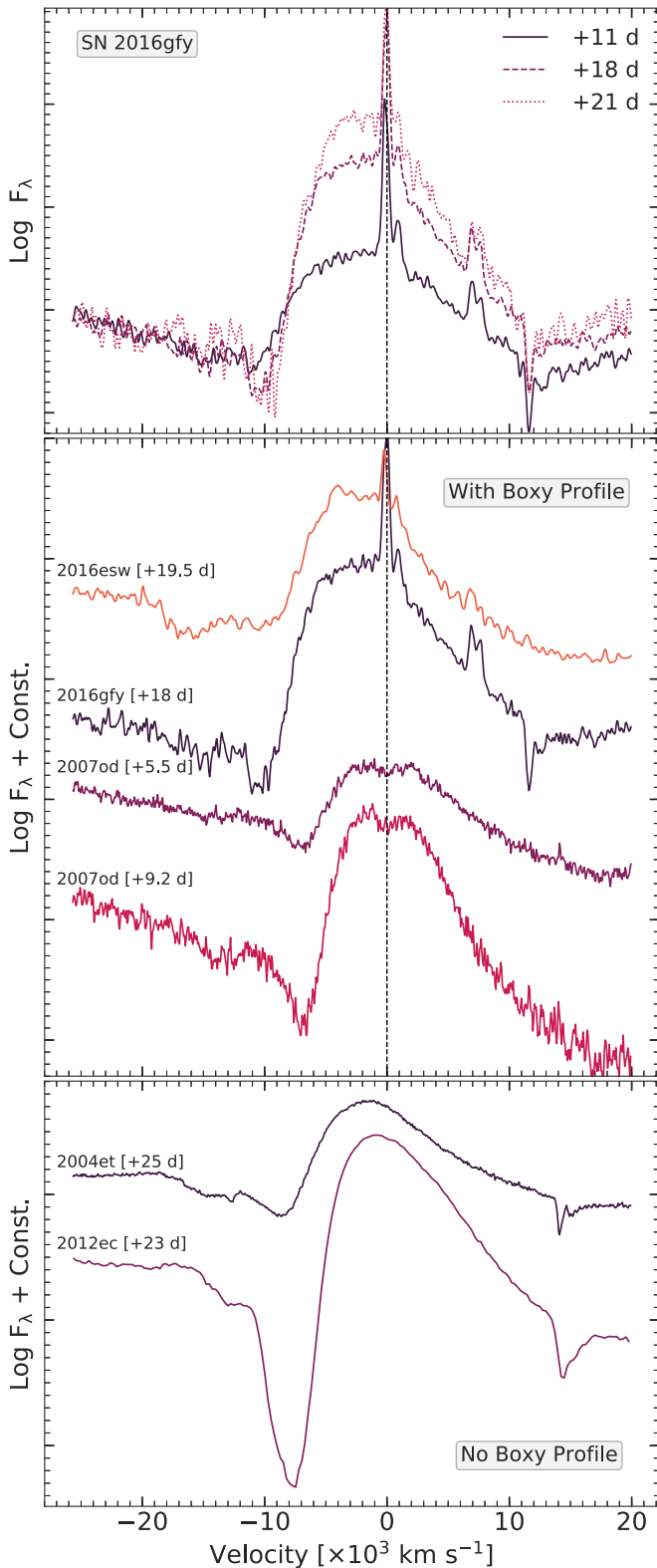


Figure 20. Top panel: boxy profile of $H\alpha$ seen in the spectra of SN 2016gfy from ~ 11 –21 days. Middle panel: comparison with SNe II that show boxy emission profile: SN 2007od (Inserra et al. 2011) and SN 2016esw (de Jaeger et al. 2018b). Bottom panel: SNe II that show no boxy profile have been shown for reference: 2004et (Sahu et al. 2006) and 2012ec (Barbarino et al. 2015).

The top panel in Figure 23 shows the comparison during the late-plateau phase. The lack of richness in the metal features in the spectra of SN 2016gfy coupled with their weakness is

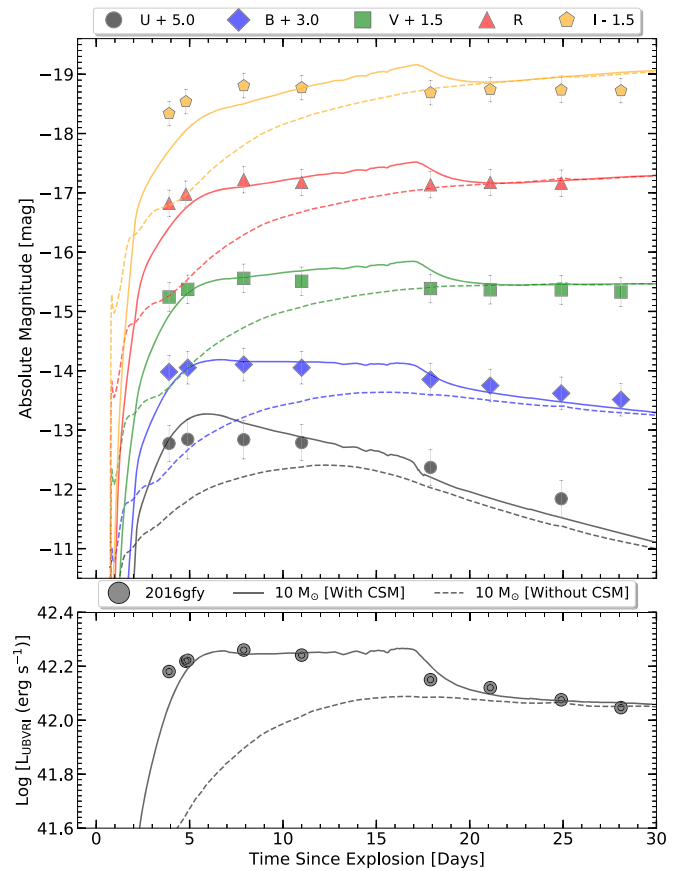


Figure 21. Comparison of SN 2016gfy with the $10 M_{\odot}$ progenitor model from Sukhbold et al. (2016) with CSM (solid) and without CSM (dashed). Top panel compares the broadband absolute magnitude LCs whereas the bottom panel compares the bolometric LCs.

clearly evident. Hence, the inference of metal-poor progenitor of SN 2016gfy is strengthened as the SN spectra traces the progenitor metallicity during the photospheric phase (A16). The comparison during the nebular phase is shown in the bottom panel of Figure 23. The spectra of SN 2016gfy shows relatively weak signatures of Na I D , $[\text{O I}] \lambda\lambda 6300, 6364$ and the $[\text{Ca II}] \lambda\lambda 7291, 7324$ and the Ca II NIR triplet. Also, absorption associated with the $H\alpha$ is almost negligible in comparison with other SNe II indicating that SN 2016gfy entered the nebular phase earlier, possibly due to a low-mass progenitor.

SN 2016gfy adds to the sample of SNe II in low-metallicity environments (Polshaw et al. 2016; Gutiérrez et al. 2018; Meza et al. 2018; Singh et al. 2018) which were earlier considered scarce. To picture SN 2016gfy in the parameter space of well-studied SNe II from the literature (Hamuy 2003; Spiro et al. 2014; Valenti et al. 2015; Singh et al. 2018), the absolute V -band magnitude during the mid-plateau is compared with the mass of ^{56}Ni synthesized in Figure 24. SN 2016gfy lies within the 3σ dispersion of the fit shown and indicates no peculiarity w.r.t. these parameters.

The plateau decline rates, s_1 and s_2 (Anderson et al. 2014), in $UBVRI$ were determined by a linear piece-wise fit to the LCs until the end of the plateau phase (~ 90 days). When the estimated decline rates of SN 2016gfy are compared versus the extensive sample of SNe II from Anderson et al. (2014) in Figure 25, SN 2016gfy clearly stands outside the 3σ dispersion of the fit and shows extremely slow decline in comparison to

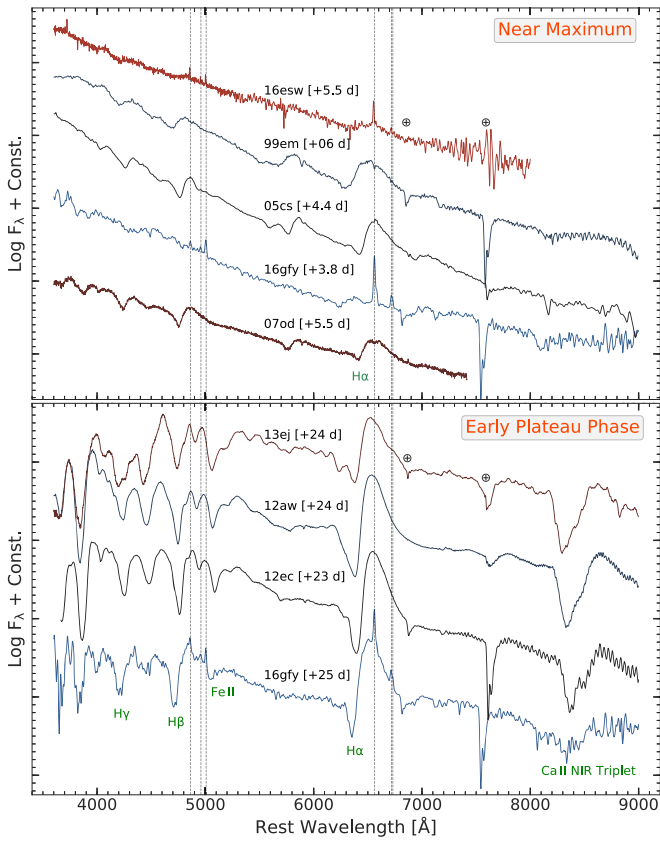


Figure 22. Comparison of the first week (~ 4 days) and early plateau phase (~ 25 days) spectra of SN 2016gfy with other SNe II in the top and bottom panels, respectively. Host galactic lines are indicated with a vertical dashed line. References: 1999em (Leonard et al. 2002a); 2005cs (Pastorello et al. 2009); 2007od (Inserra et al. 2011); 2012aw (Bose et al. 2013); 2012ec (Barbarino et al. 2015); 2013ej (Bose et al. 2015a); 2016esw (de Jaeger et al. 2018b).

SNe of similar luminosity. SN 2016gfy has decline rates of $s_1 = 0.94 \text{ mag (100 day)}^{-1}$ and $s_2 = 0.12 \text{ mag (100 day)}^{-1}$ in the plateau and are much lower than the mean decline rates for SNe II in Anderson et al. (2014), which have $s_1^{\text{mean}} \sim 2.65 \text{ mag (100 day)}^{-1}$ and $s_2^{\text{mean}} \sim 1.27 \text{ mag (100 day)}^{-1}$. As discussed in Section 8.2, the effect of ^{56}Ni and its mixing on the bolometric LC of SN 2016gfy is significant and is clearly evident in the comparison.

However, if the change in slope of $\sim 1 \text{ mag (100 day)}^{-1}$ due to the effect of ^{56}Ni is taken into account, SN 2016gfy (shown as a gray circle) lies directly on the expected correlation from the fits. It appears that the diversity of decline rates seen in SNe II is not only due to the range of envelope masses seen for progenitors of different masses but also due to varied amounts of ^{56}Ni synthesized and its degree of mixing. The effects of ^{56}Ni -mixing and the weak metal features in the spectra of SN 2016gfy indicate a metallicity at the lower end of the population of SNe II, making SN 2016gfy atypical and an interesting object to study.

9. Summary

In this article, we presented the photometric and spectroscopic analyses of the slow-declining Type II SN 2016gfy. The properties of SN 2016gfy are outlined below:

1. SN 2016gfy is a luminous SN II with a peak V -band absolute magnitude of $-17.06 \pm 0.24 \text{ mag}$.

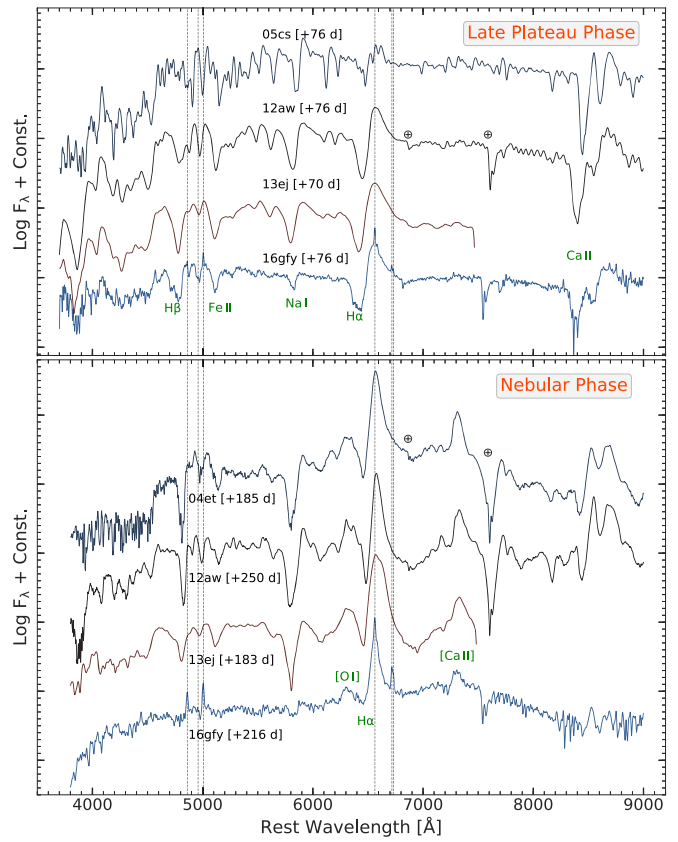


Figure 23. Comparison of the late-plateau (~ 76 days) and nebular phase (~ 216 days) spectra of SN 2016gfy with other SNe II in the top and bottom panels, respectively. Host galactic lines are indicated with a vertical dashed line. References: 2004et (Sahu et al. 2006); 2005cs (Pastorello et al. 2009); 2012aw (Bose et al. 2013); 2013ej (Bose et al. 2015a).

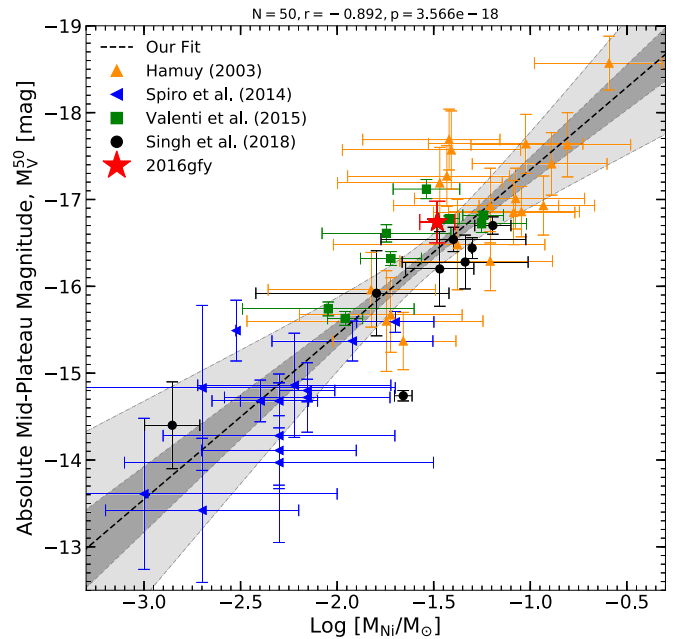


Figure 24. Plot of M_V^{50} vs. $\text{Log } M_{\text{Ni}}$, a correlation inferred by Hamuy (2003) for SNe II. The data is adopted from Hamuy (2003), Spiro et al. (2014), Valenti et al. (2015), and Singh et al. (2018). The fits to the collective sample are shown with a dotted line. The 1σ and 3σ confidence intervals of the fit are shaded in dark gray and light gray, respectively.

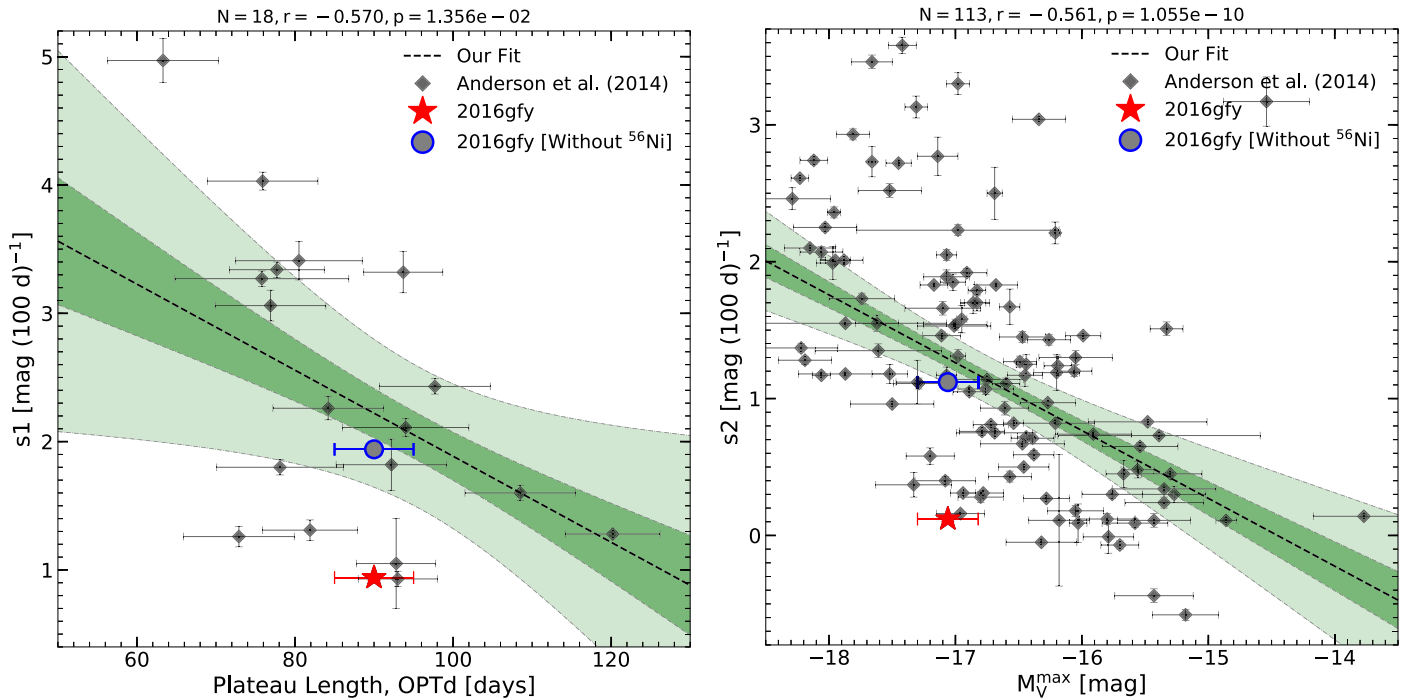


Figure 25. Decline rates s_1 and s_2 plotted against the plateau length (OPTd) and M_V^{Max} , respectively. The sample for the comparison is adopted from Anderson et al. (2014). The dashed line shows the fit to the sample with the 1σ and 3σ confidence intervals shown shaded in dark and light, respectively.

2. It is a slow-declining SN II ($s_1 = 0.94 \text{ mag (100 day)}^{-1}$ and $s_2 = 0.12 \text{ mag (100 day)}^{-1}$) in comparison to the extensive sample of SNe II in Anderson et al. (2014).
3. The host galaxy NGC 2276 is a starburst with an SFR $\sim 8.5 M_\odot \text{ yr}^{-1}$. The spectrum of the parent H II region yielded an oxygen abundance of $12 + \log(\text{O}/\text{H}) = 8.50 \pm 0.11$, indicating an average metallicity for its progenitor in comparison to the sample of SNe II (Anderson et al. 2016).
4. The progenitor of SN 2016gfy belongs to the class of RSGs with a radius in the range of $\sim 350\text{--}700 R_\odot$. The progenitor has a mass in the range of $12\text{--}15 M_\odot$ and an explosion energy in the range of $(0.9\text{--}1.4) \times 10^{51} \text{ erg}$.
5. A boxy emission profile of $\text{H}\alpha$ is seen in the spectra obtained during $\sim 11\text{--}21$ days indicating a CSM–ejecta interaction. This CSM, in the immediate vicinity of the SN could be a result of the mass-loss episode 30–80 yr before the explosion. Numerical modeling of SN 2016gfy suggests the presence of $0.15 M_\odot$ CSM spread to a radius of $\sim 70 \text{ au}$ around the progenitor.
6. The late-plateau phase ($\sim 50\text{--}95$ days) in SN 2016gfy shows a bump that is explained as a result of interaction with the CSM and/or partial mixing of ^{56}Ni in the SN ejecta.
7. The spectral evolution of SN 2016gfy features metal-poor spectra compared to other SNe II and the theoretical models of Dessart et al. (2013), signifying a low metallicity of the progenitor and is consistent with the low metallicity of the parent H II region.

We thank the anonymous referee for insightful suggestions. We thank Dr. Thomas de Jaeger and Nicolas Eduardo Meza for sharing data. We would also like to thank Dr. Sudhanshu Barway for discussions involving metallicity estimation of galaxies and galaxy morphology.

We thank the staff of IAO, Hanle, and CREST, Hosakote, that made these observations possible. The facilities at IAO and

CREST are operated by the Indian Institute of Astrophysics, Bangalore. Observations reported here were also obtained at the MMT Observatory, a joint facility of the University of Arizona and the Smithsonian Institution. We also thank the observers who helped us with the follow-up observations. B.K. acknowledges the Science and Engineering Research Board (SERB) under the Department of Science & Technology (DST), Govt. of India, for financial assistance in the form of National Post-Doctoral Fellowship (Ref. no. PDF/2016/001563). B.K., D.K.S., and G.C.A. acknowledge the BRICS grant, DST/IMRCD/BRICS/PilotCall1/MuMeSTU/2017(G), for the present work. D.K.S. and G.C.A. also acknowledge the DST/JSPS grant, DST/INT/JSPS/P/281/2018.

This research made use of REDPIPE,⁹ an assemblage of data reduction and analysis scripts written by A.S. This work also made use of the NASA Astrophysics Data System and the NASA/IPAC Extragalactic Database (NED),¹⁰ which is operated by the Jet Propulsion Laboratory, California Institute of Technology. We acknowledge Wiezmann Interactive Supernova data REpository¹¹ (WiSeREP; Yaron & Gal-Yam 2012).

Software: SciPy (v1.3.0, Oliphant 2007), Matplotlib (v3.1.0, Hunter 2007), Pandas (v0.24.2, McKinney 2010), PyRAF (v2.1.14, Science Software Branch at STScI 2012), Astropy (v3.1.2, Astropy Collaboration et al. 2018), Seaborn (v0.9.0, Waskom et al. 2018).

Appendix A Comparison Sample

The sample of SNe II chosen to compare the properties of SN2016gfy is tabulated in Table 5.

⁹ <https://github.com/sPaMFouR/RedPipe>

¹⁰ <https://ned.ipac.caltech.edu>

¹¹ <https://wiserep.weizmann.ac.il>

Table 5
Comparison Sample of SNe II

SN (Name)	Explosion Epoch (JD)	Distance (Mpc)	M_{50}^V (mag)	M_{Ni} (M_{\odot})	Reference
1987A	2446859.82	0.04 ± 0.003	...	0.075 ± 0.005	1, 16
1999em	2451475.60	11.70 ± 0.99	-15.90 ± 0.20	$0.042_{0.019}^{0.027}$	2, 3, 17
2004et	2453270.25	5.60 ± 0.10	-17.14 ± 0.10	0.060 ± 0.020	4
2005cs	2453549.00	8.90 ± 0.50	-14.83 ± 0.10	0.006 ± 0.003	5, 18
2007od	2454404.00	25.70 ± 0.80	-17.64 ± 0.22	0.003	6
2009ib	2455041.30	19.80 ± 2.80	...	0.046 ± 0.015	7
2012aw	2456002.59	9.90 ± 0.10	-16.67 ± 0.04	0.056 ± 0.013	8, 13
2012ec	2456143.00	17.30 ± 0.96	-16.54 ± 0.14	0.040 ± 0.015	9
2013ab	2456340.00	24.30 ± 1.00	-16.70 ± 0.10	0.064 ± 0.006	10
2013ej	2456497.30	9.57 ± 0.70	-16.60 ± 0.10	0.018 ± 0.006	11, 13
ASASSN-14dq	2456841.50	44.80 ± 3.10	-16.90 ± 0.20	0.029 ± 0.005	12
2014cx	2456901.89	22.28 ± 1.60	-17.20 ± 0.20	0.056 ± 0.008	13
2016X	2457405.92	15.20 ± 3.30	-16.20 ± 0.43	0.034 ± 0.006	14
2016esw	2457608.33	123.60	-17.35 ± 0.11	...	15

References. (1) Hamuy & Suntzeff (1990); (2) Leonard et al. (2002a); (3) Leonard et al. (2003); (4) Sahu et al. (2006); (5) Pastorello et al. (2009); (6) Inserra et al. (2011); (7) Takáts et al. (2015); (8) Bose et al. (2013); (9) Barbarino et al. (2015); (10) Bose et al. (2015b); (11) Bose et al. (2015a); (12) Singh et al. (2018); (13) Valenti et al. (2015); (14) Huang et al. (2018); (15) de Jaeger et al. (2018b); (16) Turatto et al. (2003); (17) Hamuy et al. (2001); (18) Spiro et al. (2014).

Appendix B Template Subtraction

Since SN 2016gfy exploded in the bright spiral arm of the host galaxy, there is a significant contribution from the host environment in its optical photometry (see Figure 26). Template images of NGC 2276 were obtained in a good seeing condition

($\leq 2''$) from the 2 m HCT on 2018 February 13, almost 1.5 yr from the date of explosion when the SN had diminished enough to allow for the the imaging of the bright galaxy background. The templates were aligned to the object frame, PSF-matched, background-subtracted, and scaled in order to subtract the host galaxy contribution in the photometric frames of the SN 2016gfy.

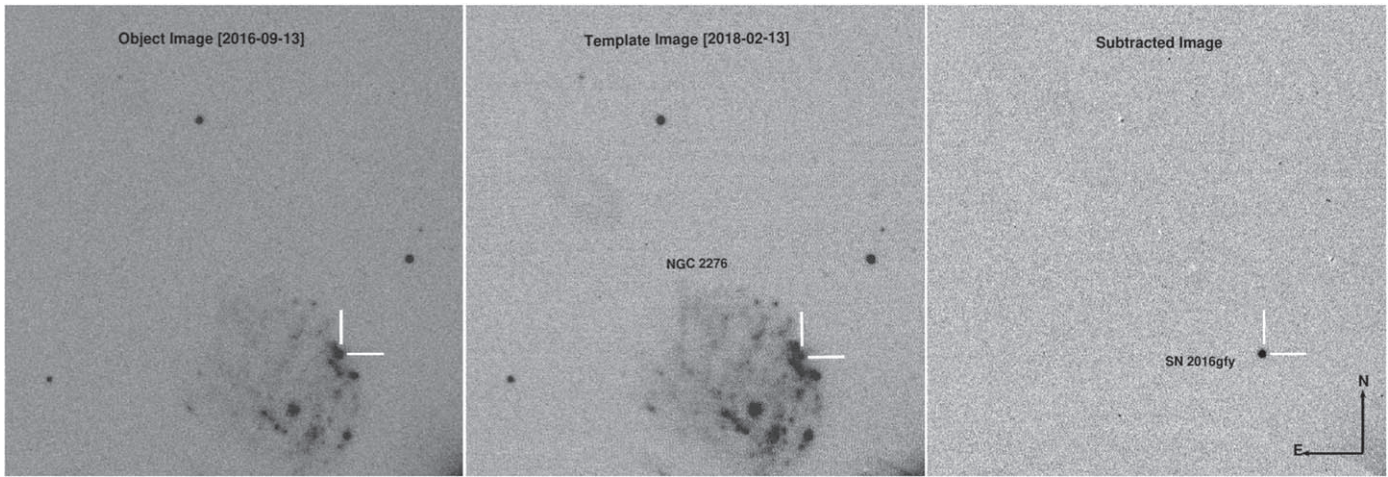


Figure 26. Left panel: U -band image of SN 2016gfy obtained with the HCT on 2016 September 13. Middle panel: template image observed with HCT on 2018 February 13. Right panel: subtracted image procured after PSF-matching of the background-subtracted images in the first two panels.

Appendix C Distance Estimation Using SCM

SNe Ia have been studied up to a redshift of ~ 1.7 (Rubin et al. 2013). To allow the study beyond the above redshift, wherein SNe II are in abundance due to their shorter lifetimes and hence becomes an entrancing choice even though they are fainter. The SCM (Hamuy & Pinto 2002), helps estimate distance using the correlation of bolometric luminosity with the expansion velocity of the ejecta during the plateau phase. The latest value of the Hubble constant determined by SNe Ia, i.e., $H_0 = 73.52 \pm 1.62 \text{ km s}^{-1} \text{ Mpc}^{-1}$ (Riess et al. 2018) is used here to compute the distances. The implementation of these techniques is discussed in the following subsections.

C.1. Apparent LC Fits

The apparent $BVRI$ LCs of SN 2016gfy were fit using an analytic function (Olivares et al. 2010) comprising of three components (see Equation (6)). Nelder–Mead optimization was employed to minimize the χ^2 of the fit. The interpolated magnitudes from the fit were extracted at a step size of 1 day until 250 days and the 3σ deviation of the fit were adopted as errors. The quantities inferred from the fit are compiled in Table 6. The parameter t_{PT} derived here can be used as an alternative to the date of explosion to define the epoch for calculating observables for the SCM

$$f(t) = \underbrace{\frac{-a_0}{1 + e^{(t-t_{PT})/w_0}}}_{\text{Fermi-Dirac term}} + \underbrace{p_0(t - t_{PT}) + m_0}_{\text{Linear term}} - \underbrace{P e^{-\left(\frac{t-Q}{R}\right)^2}}_{\text{Gaussian term}}. \quad (6)$$

C.2. Expansion Velocities

Photospheric velocities measured from the minimum of the of Fe II $\lambda 5169$ absorption are accurate up to 5%–10% (Dessart & Hillier 2005). An alternative is to use the H β feature, which has a higher SNR and correlates as $v_{\text{Fe II}} = (0.82 \pm 0.05) v_{\text{H}\beta}$ during the plateau phase (Poznanski et al. 2010; Takáts & Vinkó 2012). A power law ($v(t) = \alpha \times (t - A)^\beta$) is fit to the

Fe II $\lambda 5169$ velocity curve during the plateau phase (until the time of inflection, ~ 110 days), where α , A , and β have no direct physical interpretations. The variance-weighted least squares minimization (WLS) fit is shown in an inset in Figure 15 and helped extract expansion velocities from 20 to 110 days at an interval of 1 day without the need for extrapolation. The errors computed are the 3σ deviations of the fit.

C.3. Color Evolution Fits

The Galactic extinction corrected colors $U - B$, $B - V$, $V - R$, and $V - I$ were fitted with a Legendre polynomial until 150 days from the date of the explosion, some of which are shown in Figure 8 with a red dashed line. The color values were obtained in a continuous grid with a spacing of 1 day until the transition phase (~ 110 days).

C.4. Methodology

The SCM technique was further inspected by Hamuy (2004), Nugent et al. (2006), Poznanski et al. (2009), and Olivares et al. (2010; hereafter H04, N06, P09, and O10, respectively) using different samples of SNe II and using distinct epochs as reference for computing the correlated quantities.

1. Hamuy (2004): H04 investigated the SCM technique with a sample of 24 SNe II and found that SCM has a precision of 15%. H04 used a reference epoch of 50 days from the date of explosion to measure the SN observables required for SCM and estimated the distances using Equation (7).
2. Nugent et al. (2006): N06 utilized the $(V - I)$ color during the mid-plateau phase (~ 50 days) to perform reddening correction using the extinction law from Cardelli et al. (1989). They adopted an unreddened $V - I$ color of 0.53 mag for SNe II and used an $H_0 = 70 \text{ km s}^{-1} \text{ Mpc}^{-1}$ for computing the distances using Equation (8).
3. Poznanski et al. (2009): P09 remodeled the relation from N06 with a sample of 34 SNe II with the most tangible assumption that not all the SNe must follow the same extinction law as Cardelli et al. (1989). The value of β used here differs from the value in P09 because of the

Table 6
Parameters Extracted from the Analytic Fit (Olivares et al. 2010) *BVRI* LC of SN 2016gfy

Filter	a_0 (mag)	t_{PT} (days) ^a	w_0 (days)	p_0 (mag/day)	m_0 (mag)	P (mag)	Q (days)	R (days)	s_1^b (mag/100 days)	s_2^b (mag/100 days)
<i>B</i>	2.19 ± 0.04	107.4 ± 0.8	8.79 ± 1.39	0.0059	19.79	0.92	4.24	27.37	3.10	1.15
<i>V</i>	1.16 ± 0.01	113.2 ± 0.5	2.65 ± 0.34	0.0107	18.27	0.50	82.37	31.39	0.94	0.12
<i>R</i>	1.42 ± 0.01	112.9 ± 0.3	3.67 ± 0.31	0.0086	17.35	-0.59	11.25	52.77	0.30	-0.02
<i>I</i>	1.25 ± 0.01	114.0 ± 0.5	3.54 ± 0.42	0.0109	16.84	-0.98	7.65	53.64	0.11	-0.27

Notes.^a Time since explosion epoch (JD 2,457,641.40).^b Extracted from a linear piece-wise fit to the light curves.

Table 7
Distances to the Host Galaxy NGC 2276

Distance Method	Distance (in Mpc)	Distance Modulus (in mag)	Reference
Hubble Flow Distance (Virgo + GA + Shapley)	37.1 ± 2.6	32.85 ± 0.15	2
CO-Line Tully–Fisher relation	22.6	31.77	3
Luminosity Distance	33.1	32.60	1
Mean SCM	29.64 ± 2.65	32.36 ± 0.18	1

References. (1) This paper; (2) Mould et al. (2000); (3) Schoniger & Sofue (1994).

different value of H_0 adopted here instead of $H_0 = 70 \text{ km s}^{-1} \text{ Mpc}^{-1}$ in P09. P09 computed the distances using Equation (9).

4. Olivares et al. (2010): The refined SCM method by O10 makes use of the expansion velocities, magnitudes, and color terms estimated 30 days before the middle of the transition phase and was calibrated using a sample of 37 SNe II. The calibrated relation for *BVI* bands is given in Equation (10).

$$5 \log[H_0 D_\lambda] = m_\lambda - A_\lambda + \alpha \times \log[v_{\text{Fe II}}/5000] + \beta \quad (7)$$



$$5 \log[D_\lambda] - 5 = m_\lambda + \alpha \times \log[v_{\text{Fe II}}/5000] + \gamma[(V - I) - 0.53] - \beta \quad (8)$$

$$5 \log[H_0 D_\lambda] = m_\lambda + \alpha \times \log[v_{\text{Fe II}}/5000] - \gamma[(V - I) - 0.53] - \beta \quad (9)$$

$$5 \log[H_0 D_\lambda] = m_\lambda + \alpha \times \log[v_{\text{Fe II}}/5000] - \gamma(V - I) - \beta, \quad (10)$$

where m_λ is the apparent magnitude, A_λ is the extinction, $v_{\text{Fe II}}$ is in km s^{-1} , D_λ is in Mpc, and α , β , and γ are dimensionless constants mentioned in Table 2. A summary of distances obtained for NGC 2276 is shown in Table 7.

ORCID iDs

Avinash Singh  <https://orcid.org/0000-0003-2091-622X>
 Brajesh Kumar  <https://orcid.org/0000-0001-7225-2475>
 Takashi J. Moriya  <https://orcid.org/0000-0003-1169-1954>
 G. C. Anupama  <https://orcid.org/0000-0003-3533-7183>
 Peter J. Brown  <https://orcid.org/0000-0001-6272-5507>
 Jennifer E. Andrews  <https://orcid.org/0000-0003-0123-0062>

References

- Anderson, J. P., González-Gaitán, S., Hamuy, M., et al. 2014, *ApJ*, 786, 67
 Anderson, J. P., Gutiérrez, C. P., Dessart, L., et al. 2016, *A&A*, 589, A110
 Andrews, J. E., Gallagher, J. S., Clayton, G. C., et al. 2010, *ApJ*, 715, 541
 Andrews, J. E., & Smith, N. 2018, *MNRAS*, 477, 74
 Arcavi, I., Gal-Yam, A., Cenko, S. B., et al. 2012, *ApJL*, 756, L30
 Arcavi, I., Howell, D. A., Kasen, D., et al. 2017, *Natur*, 551, 210
 Arnett, W. D. 1980, *ApJ*, 237, 541
 Arnett, W. D. 1982, *ApJ*, 253, 785
 Asplund, M., Grevesse, N., Sauval, A. J., & Scott, P. 2009, *ARA&A*, 47, 481
 Astropy Collaboration, Price-Whelan, A. M., Sipőcz, B. M., et al. 2018, *AJ*, 156, 123
 Baldwin, J. A., Phillips, M. M., & Terlevich, R. 1981, *PASP*, 93, 5
 Barbarino, C., Dall’Ora, M., Botticella, M. T., et al. 2015, *MNRAS*, 448, 2312
 Barbon, R., Ciatti, F., & Rosino, L. 1979, *A&A*, 72, 287
 Bersten, M. C., Benvenuto, O., & Hamuy, M. 2011, *ApJ*, 729, 61
 Blinnikov, S., Lundqvist, P., Bartunov, O., Nomoto, K., & Iwamoto, K. 2000, *ApJ*, 532, 1132
 Blinnikov, S. I., & Bartunov, O. S. 1993, *A&A*, 273, 106
 Blinnikov, S. I., Eastman, R., Bartunov, O. S., Popolitov, V. A., & Woosley, S. E. 1998, *ApJ*, 496, 454
 Blinnikov, S. I., Röpke, F. K., Sorokina, E. I., et al. 2006, *A&A*, 453, 229
 Bose, S., & Kumar, B. 2014, *ApJ*, 782, 98
 Bose, S., Kumar, B., Sutaria, F., et al. 2013, *MNRAS*, 433, 1871
 Bose, S., Sutaria, F., Kumar, B., et al. 2015a, *ApJ*, 806, 160
 Bose, S., Valenti, S., Misra, K., et al. 2015b, *MNRAS*, 450, 2373
 Bradley, L., Sipocz, B., Robitaille, T., et al. 2017, *astropy/photutils*, v0.4, Zenodo, doi:10.5281/zenodo.1039309
 Breeveld, A. A., Landsman, W., Holland, S. T., et al. 2011, in *AIP Conf. Ser.* 1358, *Gamma Ray Bursts 2010*, ed. J. E. McEnery, J. L. Racusin, & N. Gehrels (Melville, NY: AIP), 373
 Brown, P. J., Breeveld, A. A., Holland, S., Kuin, P., & Pritchard, T. 2014, *A&SS*, 354, 89
 Brown, P. J., Dessart, L., Holland, S. T., et al. 2007, *ApJ*, 659, 1488
 Cardelli, J. A., Clayton, G. C., & Mathis, J. S. 1989, *ApJ*, 345, 245
 Chabrier, G. 2003, *PASP*, 115, 763
 Chevalier, R. A., & Fransson, C. 1994, *ApJ*, 420, 268
 Chugai, N. N. 1994, *ApJL*, 428, L17
 Chugai, N. N., Chevalier, R. A., & Utrobin, V. P. 2007, *ApJ*, 662, 1136
 Colgate, S. A. 1974, *ApJ*, 187, 333
 Cowen, D. F., Franckowiak, A., & Kowalski, M. 2010, *Aph*, 33, 19

- Das, S., & Ray, A. 2017, *ApJ*, **851**, 138
- Davies, B., & Beasor, E. R. 2018, *MNRAS*, **474**, 2116
- Davis, D. S., Keel, W. C., Mulchaey, J. S., & Henning, P. A. 1997, *AJ*, **114**, 613
- de Jaeger, T., Anderson, J. P., Galbany, L., et al. 2018a, *MNRAS*, **476**, 4592
- de Jaeger, T., Galbany, L., Gutiérrez, C. P., et al. 2018b, *MNRAS*, **478**, 3776
- de Jaeger, T., González-Gaitán, S., Anderson, J. P., et al. 2015, *ApJ*, **815**, 121
- Dessart, L., Gutierrez, C. P., Hamuy, M., et al. 2014, *MNRAS*, **440**, 1856
- Dessart, L., & Hillier, D. J. 2005, *A&A*, **439**, 671
- Dessart, L., Hillier, D. J., Waldman, R., & Livne, E. 2013, *MNRAS*, **433**, 1745
- de Vaucouleurs, G., de Vaucouleurs, A., Corwin, H. G., Jr., et al. 1991, Third Reference Catalogue of Bright Galaxies. Vol. I, II, III (New York: Springer)
- Dickinson, M., Papovich, C., Ferguson, H. C., & Budavári, T. 2003, *ApJ*, **587**, 25
- Dimai, A. 2016, Transient Name Server Discovery Report, 673
- Dimai, A., Migliardi, M., & Manzini, F. 2005, *IAUC*, **8588**, 2
- Domínguez, A., Siana, B., Henry, A. L., et al. 2013, *ApJ*, **763**, 145
- Eldridge, J. J., Stanway, E. R., Xiao, L., et al. 2017, *PASA*, **34**, e058
- Elias-Rosa, N., Van Dyk, S. D., Li, W., et al. 2011, *ApJ*, **742**, 6
- Elmhamdi, A., Chugai, N. N., & Danziger, I. J. 2003a, *A&A*, **404**, 1077
- Elmhamdi, A., Danziger, I. J., Chugai, N., et al. 2003b, *MNRAS*, **338**, 939
- Epinat, B., Amram, P., & Marcelin, M. 2008, *MNRAS*, **390**, 466
- Falk, S. W., & Arnett, W. D. 1977, *ApJS*, **33**, 515
- Faran, T., Poznanski, D., Filippenko, A. V., et al. 2014a, *MNRAS*, **445**, 554
- Faran, T., Poznanski, D., Filippenko, A. V., et al. 2014b, *MNRAS*, **442**, 844
- Filippenko, A. V. 1982, *PASP*, **94**, 715
- Filippenko, A. V. 1997, *ARA&A*, **35**, 309
- Fitzpatrick, E. L. 1999, *PASP*, **111**, 63
- Forster, F., Moriya, T. J., Maureira, J. C., et al. 2018, *NatAs*, **2**, 808
- Fransson, C., & Chevalier, R. A. 1989, *ApJ*, **343**, 323
- Gall, E. E. E., Polshaw, J., Kotak, R., et al. 2015, *A&A*, **582**, A3
- Gehrels, N., Chincarini, G., Giommi, P., et al. 2004, *ApJ*, **611**, 1005
- González-Gaitán, S., Tominaga, N., Molina, J., et al. 2015, *MNRAS*, **451**, 2212
- Gutiérrez, C. P., Anderson, J. P., Hamuy, M., et al. 2017, *ApJ*, **850**, 89
- Gutiérrez, C. P., Anderson, J. P., Sullivan, M., et al. 2018, *MNRAS*, **479**, 3232
- Hamuy, M. 2003, *ApJ*, **582**, 905
- Hamuy, M. 2004, in *Measuring and Modeling the Universe 2*, ed. W. L. Freedman (Cambridge: Cambridge Univ. Press), 2
- Hamuy, M., & Pinto, P. A. 2002, *ApJL*, **566**, L63
- Hamuy, M., Pinto, P. A., Maza, J., et al. 2001, *ApJ*, **558**, 615
- Hamuy, M., & Suntzeff, N. B. 1990, *AJ*, **99**, 1146
- Heger, A., Fryer, C. L., Woosley, S. E., Langer, N., & Hartmann, D. H. 2003, *ApJ*, **591**, 288
- Henry, R. B. C., & Worthey, G. 1999, *PASP*, **111**, 919
- Horiuchi, S., Nakamura, K., Takiwaki, T., Kotake, K., & Tanaka, M. 2014, *MNRAS*, **445**, L99
- Huang, F., Wang, X.-F., Hosseinzadeh, G., et al. 2018, *MNRAS*, **475**, 3959
- Hunter, J. D. 2007, *CSE*, **9**, 90
- Inserra, C., Turatto, M., Pastorello, A., et al. 2011, *MNRAS*, **417**, 261
- Iskudarian, S. G. 1968, *ATsir*, **480**, 1
- Iskudaryan, S. G., & Shakhbazyan, R. K. 1967, *Ap*, **3**, 67
- Jerkstrand, A., Fransson, C., Maguire, K., et al. 2012, *A&A*, **546**, A28
- Jerkstrand, A., Smartt, S. J., Fraser, M., et al. 2014, *MNRAS*, **439**, 3694
- Jordi, K., Grebel, E. K., & Ammon, K. 2006, *A&A*, **460**, 339
- Karachentsev, I. D., & Kaisina, E. I. 2013, *AJ*, **146**, 46
- Kasen, D., & Woosley, S. E. 2009, *ApJ*, **703**, 2205
- Kauffmann, G., Heckman, T. M., Tremonti, C., et al. 2003, *MNRAS*, **346**, 1055
- Kennicutt, R. C., Jr. 1984, *ApJ*, **277**, 361
- Kennicutt, R. C., Jr. 1998, *ARA&A*, **36**, 189
- Khazov, D., Yaron, O., Gal-Yam, A., et al. 2016, *ApJ*, **818**, 3
- Kirshner, R. P., & Kwan, J. 1974, *ApJ*, **193**, 27
- Kochanek, C. S., Khan, R., & Dai, X. 2012, *ApJ*, **759**, 20
- Kozyreva, A., Nakar, E., & Waldman, R. 2019, *MNRAS*, **483**, 1211
- Kumar, B., Singh, A., Srivastav, S., Sahu, D. K., & Anupama, G. C. 2018, *MNRAS*, **473**, 3776
- Kuncarayakti, H., Doi, M., Aldering, G., et al. 2013a, *AJ*, **146**, 30
- Kuncarayakti, H., Doi, M., Aldering, G., et al. 2013b, *AJ*, **146**, 31
- Kuncarayakti, H., Reynolds, T., Mattila, S., et al. 2016, *ATel*, **9498**, 1
- Landolt, A. U. 1992, *AJ*, **104**, 340
- Leonard, D. C., Filippenko, A. V., Gates, E. L., et al. 2002a, *PASP*, **114**, 35
- Leonard, D. C., Filippenko, A. V., Li, W., et al. 2002b, *AJ*, **124**, 2490
- Leonard, D. C., Kanbur, S. M., Ngeow, C. C., & Tanvir, N. R. 2003, *ApJ*, **594**, 247
- Li, W., Leaman, J., Chornock, R., et al. 2011, *MNRAS*, **412**, 1441
- Litvinova, I. Y., & Nadezhin, D. K. 1985, *SvAL*, **11**, 145
- Lovegrove, E., & Woosley, S. E. 2013, *ApJ*, **769**, 109
- Maguire, K., Di Carlo, E., Smartt, S. J., et al. 2010, *MNRAS*, **404**, 981
- McCall, M. L. 2004, *AJ*, **128**, 2144
- McKinney, W. 2010, in *Proc. 9th Python in Science Conf.*, ed. S. van der Walt & J. Millman (SciPy), 51
- Meza, N., Prieto, J. L., Clocchiatti, A., et al. 2018, arXiv:1811.11771
- Minkowski, R. 1941, *PASP*, **53**, 224
- Moriya, T. J., Förster, F., Yoon, S.-C., Gräfenor, G., & Blinnikov, S. I. 2018, *MNRAS*, **476**, 2840
- Moriya, T. J., Yoon, S.-C., Gräfenor, G., & Blinnikov, S. I. 2017, *MNRAS*, **469**, L108
- Morozova, V., Piro, A. L., Renzo, M., et al. 2015, *ApJ*, **814**, 63
- Morozova, V., Piro, A. L., Renzo, M., & Ott, C. D. 2016, *ApJ*, **829**, 109
- Morozova, V., Piro, A. L., & Valenti, S. 2017, *ApJ*, **838**, 28
- Morrissey, P., Conrow, T., Barlow, T. A., et al. 2007, *ApJS*, **173**, 682
- Mould, J. R., Huchra, J. P., Freedman, W. L., et al. 2000, *ApJ*, **529**, 786
- Nagy, A. P., Ordasi, A., Vinkó, J., & Wheeler, J. C. 2014, *A&A*, **571**, A77
- Nagy, A. P., & Vinkó, J. 2016, *A&A*, **589**, A53
- Nakaoka, T., Kawabata, K. S., Maeda, K., et al. 2018, *ApJ*, **859**, 78
- Nakar, E., Poznanski, D., & Katz, B. 2016, *ApJ*, **823**, 127
- Nugent, P., Sullivan, M., Ellis, R., et al. 2006, *ApJ*, **645**, 841
- Oke, J. B., & Gunn, J. E. 1983, *ApJ*, **266**, 713
- Oliphant, T. E. 2007, *CSE*, **9**, 10
- Olivares, F., Hamuy, M., Pignata, G., et al. 2010, *ApJ*, **715**, 833
- Osterbrock, D. E. 1989, *Astrophysics of Gaseous Nebulae and Active Galactic Nuclei* (Mill Valley, CA: Univ. Science Books)
- Pastorello, A., Valenti, S., Zampieri, L., et al. 2009, *MNRAS*, **394**, 2266
- Patat, F., Barbon, R., Cappellaro, E., & Turatto, M. 1994, *A&A*, **282**, 731
- Pettini, M., & Pagel, B. E. J. 2004, *MNRAS*, **348**, L59
- Polshaw, J., Kotak, R., Dessart, L., et al. 2016, *A&A*, **588**, 1
- Poznanski, D., Butler, N., Filippenko, A. V., et al. 2009, *ApJ*, **694**, 1067
- Poznanski, D., Nugent, P. E., & Filippenko, A. V. 2010, *ApJ*, **721**, 956
- Poznanski, D., Prochaska, J. X., & Bloom, J. S. 2012, *MNRAS*, **426**, 1465
- Prieto, J. L., Stanek, K. Z., & Beacom, J. F. 2008, *ApJ*, **673**, 999
- Pritchard, T. A., Roming, P. W. A., Brown, P. J., Bayless, A. J., & Frey, L. H. 2014, *ApJ*, **787**, 157
- Quataert, E., & Shiode, J. 2012, *MNRAS*, **423**, L92
- Rabinak, I., & Waxman, E. 2011, *ApJ*, **728**, 63
- Rasmussen, J., Ponman, T. J., & Mulchaey, J. S. 2006, *MNRAS*, **370**, 453
- Riess, A. G., Casertano, S., Yuan, W., et al. 2018, *ApJ*, **861**, 126
- Rodríguez, Ó, Clocchiatti, A., & Hamuy, M. 2014, *AJ*, **148**, 107
- Roming, P. W. A., Kennedy, T. E., Mason, K. O., et al. 2005, *SSRv*, **120**, 95
- Rubin, D., Knop, R. A., Rykoff, E., et al. 2013, *ApJ*, **763**, 35
- Sahu, D. K., Anupama, G. C., & Chakradhari, N. K. 2013, *MNRAS*, **433**, 2
- Sahu, D. K., Anupama, G. C., Chakradhari, N. K., et al. 2018, *MNRAS*, **475**, 2591
- Sahu, D. K., Anupama, G. C., Srividya, S., & Muneer, S. 2006, *MNRAS*, **372**, 1315
- Sanders, N. E., Soderberg, A. M., Gezari, S., et al. 2015, *ApJ*, **799**, 208
- Schlaflly, E. F., & Finkbeiner, D. P. 2011, *ApJ*, **737**, 103
- Schmidt, G. D., Weymann, R. J., & Foltz, C. B. 1989, *PASP*, **101**, 713
- Schöniger, F., & Sofue, Y. 1994, *A&A*, **283**, 21
- Science Software Branch at STScI 2012, PyRAF: Python alternative for IRAF, Astrophysics Source Code Library, Science Software Branch, STScI, ascl:1207.011
- Shakhbazyan, R. K. 1968, *Ap*, **4**, 123
- Singh, A., Srivastav, S., Kumar, B., Anupama, G. C., & Sahu, D. K. 2018, *MNRAS*, **480**, 2475
- Smartt, S. J. 2009, *ARA&A*, **47**, 63
- Smith, N. 2014, *ARA&A*, **52**, 487
- Smith, N., Mauerhan, J. C., Cenko, S. B., et al. 2015, *MNRAS*, **449**, 1876
- Spiro, S., Pastorello, A., Pumo, M. L., et al. 2014, *MNRAS*, **439**, 2873
- Stanway, E. R., & Eldridge, J. J. 2018, *MNRAS*, **479**, 75
- Sukhbold, T., Ertl, T., Woosley, S. E., Brown, J. M., & Janka, H.-T. 2016, *ApJ*, **821**, 38
- Swartz, D. A., Wheeler, J. C., & Harkness, R. P. 1991, *ApJ*, **374**, 266
- Taddia, F., Sollerman, J., Fremling, K., et al. 2015, *A&A*, **580**, A131
- Takáts, K., Pignata, G., Pumo, M. L., et al. 2015, *MNRAS*, **450**, 3137
- Takáts, K., & Vinkó, J. 2012, *MNRAS*, **419**, 2783
- Terrerán, G., Jerkstrand, A., Benetti, S., et al. 2016, *MNRAS*, **462**, 137
- Tomčić, N., Hughes, A., Kreckel, K., et al. 2018, *ApJL*, **869**, L38
- Treffers, R. R., Filippenko, A. V., Leibundgut, B., et al. 1993, *IAUC*, **5850**, 1
- Turatto, M., Benetti, S., & Cappellaro, E. 2003, in *From Twilight to Highlight: The Physics of Supernovae*, ed. W. Hillebrandt & B. Leibundgut (Berlin: Springer), 200

- Turatto, M., Mazzali, P. A., Young, T. R., et al. 1998, *ApJL*, 498, L129
- Valenti, S., Howell, D. A., Stritzinger, M. D., et al. 2016, *MNRAS*, 459, 3939
- Valenti, S., Sand, D., Stritzinger, M., et al. 2015, *MNRAS*, 448, 2608
- Van Dyk, S. D., Zheng, W., Maund, J. R., et al. 2019, *ApJ*, 875, 136
- Walmswell, J. J., & Eldridge, J. J. 2012, *MNRAS*, 419, 2054
- Waskom, M., Botvinnik, O., O’Kane, D., et al. 2018, mwaskom/seaborn, v0.9.0, Zenodo, doi:[10.5281/zenodo.1313201](https://doi.org/10.5281/zenodo.1313201)
- Waxman, E., Mészáros, P., & Campana, S. 2007, *ApJ*, 667, 351
- Wolter, A., Esposito, P., Mapelli, M., Pizzolato, F., & Ripamonti, E. 2015, *MNRAS*, 448, 781
- Woosley, S. E., & Heger, A. 2007, *PhR*, 442, 269
- Woosley, S. E., & Heger, A. 2012, *ApJ*, 752, 32
- Woosley, S. E., & Weaver, T. A. 1995, *ApJS*, 101, 181
- Yaron, O., & Gal-Yam, A. 2012, *PASP*, 124, 668
- Yuan, F., Jerkstrand, A., Valenti, S., et al. 2016, *MNRAS*, 461, 2003